RIS-Aided Wideband Holographic DFRC

TONG WEI, Graduate Student Member, IEEE
LINLONG WU, Senior Member, IEEE
KUMAR VIJAY MISHRA, Senior Member, IEEE
BHAVANI SHANKAR M. R., Senior Member, IEEE
University of Luxembourg, Luxembourg City, Luxembourg

To enable nonline-of-sight (NLoS) sensing and communications, dual-function radar-communications (DFRC) systems have recently proposed employing reconfigurable intelligent surface (RIS) as a reflector in wireless media. However, in the dense environment and higher frequencies, severe propagation and attenuation losses are a hindrance for RIS-aided DFRC systems to utilize wideband processing. To this end, we propose equipping the transceivers with a reconfigurable holographic surface (RHS). Unlike RIS, an RHS is a metasurface with an embedded connected feed deployed at the transceiver for greater control of the *radiation amplitude*. This surface is crucial for designing compact low-cost wideband wireless systems, wherein ultramassive antenna arrays are required to compensate for the losses incurred by severe attenuation and diffraction. We consider a wideband DFRC system equipped with an RHS at the transmitter and an RIS reflector in the channel. We jointly design the receive filter along with the digital, holographic, and passive beamformers to maximize the worst-case radar signal-to-interference-plus-noise ratio (SINR) while ensuring the communications SINR among all users. For the resulting nonconvex optimization problem, we develop an alternating maximization method to decouple and iteratively solve these subproblems. The resulting nonconvex optimization problem involves maximin objective, constant modulus, and difference of convex constraints. We develop an alternating maximization method to decouple and iteratively solve these subproblems. Numerical experiments demonstrate that the proposed method achieves better radar performance than non-RIS, random-RHS, and randomly configured RIS-aided DFRC systems.

Manuscript received 22 October 2023; accepted 2 March 2024. Date of publication 12 March 2024; date of current version 9 August 2024.

DOI. No. 10.1109/TAES.2024.3374272

Refereeing of this contribution was handled by C. Clemente.

This work was supported in part by Luxembourg National Research Fund (FNR) through the CORE project under C22/IS/17412681/S3, and in part by Luxembourg National Research Fund (FNR) through the CORE INTER project under C20/IS/14799710/SENCOM. An earlier version of this paper was published in 2023 IEEE International Conference on Acoustics, Speech and Signal Processing (ICASSP) [DOI: 10.1109/ICASSP49357.2023.10096158].

Authors' addresses: Tong Wei, Linglong Wu, Kumar Vijay Mishra, and Bhavani Shankar M. R. are with the Interdisciplinary Centre for Security, Reliability and Trust (SnT), University of Luxembourg, L-1855 Luxembourg City, Luxembourg, E-mail: (tong.wei@uni.lu; linlong.wu@uni.lu; kumar.mishra@ext.uni.lu; bhavani.shankar@uni.lu). *(Corresponding author: Linlong Wu.)*

© 2024 The Authors. This work is licensed under a Creative Commons Attribution 4.0 License. For more information, see https://creativecommons.org/licenses/by/4.0/

I. INTRODUCTION

Radio-frequency (RF) technologies have been constantly investigating, testing, and incorporating concepts. These mostly deal with the transmitter or the receiver, e.g., the use of multiple antenna techniques, but also with the channel, e.g., technology for the mm-Wave band [2]. A recent addition toward channel conditioning effort is the use of meta-materials-based intelligent surfaces in sensing and communications. These are largely employed in the reconfigurable mode, enabling adaptation to the environments. Conventionally, the wireless channel properties are not assumed to be controllable with systems designed to minimize their impact. The channel behavior tends to be random due to propagation aspects, reflection, diffraction, superposition etc, thereby significantly limiting the wireless systems' performance [2]. Exploiting the ability of the meta-materials to manipulate radio waves, e.g., in arbitrary aperture beamforming, reconfigurable intelligent surfaces (RIS) are being considered to overcome certain vagaries of the wireless channel [3]. These RISs comprise numerous passive or near-passive subwavelength metasurface elements [4] and are being considered, amongst others, in frequency selective and high-impedance surfaces [5], polarization conversion [6], leaky-wave antenna [7], beam focusing [8], and holographic imaging [9].

RIS is largely deployed as a reflector in wireless scenarios, offering nonline-of-sight (NLoS) paths, which has been exploited in RIS-aided sensing [10] and communications [11], [12] systems for coverage extension [13], [14], interference suppression [12], and information security [15]. While non-RIS-based NLoS radars have been studied (see, e.g., [16]), they suffer from the need for prior and accurate knowledge of the geometry of propagation environment. On the contrary, NLoS echoes are exploited by RIS-aided sensing to compensate for the direct path loss [10], [17]. In a similar vein, RIS aims to enhance the coverage by acting as a radio reflector and hence overcome the severe LoS attenuation or blockage between the base station (BS) and the multiple users (MU) [14]. There exists rich literature on the application of RIS addressing different facets of wireless communications [4], [12], [18].

With the rise of dual-function radar-communications (DFRC) systems wherein sensing and communications share resources [19], RIS is being explored for DFRC performance enhancement [20], [21]. A radar-centric approach to the design of a single-RIS-aided DFRC was considered in [22] to enhance radar signal-to-noise ratio (SNR) while facilitating single-user communications; this was extended to wideband DFRC with multiple RIS elements in [21], where the beam squint was considered. Toward catering to the practical need for discrete RIS phase shifts, a relevant

analysis for DFRC is considered in [23] and [24]. Regarding the communications-centric DFRC design, a recent example is [15], where the RIS facilitates secrecy rates maximization.

Early investigations on RIS-aided DFRC, largely driven by prevailing communication deployments, focused on narrowband sub-6-GHz frequencies. Of late, significant developments to exploit the large operational bandwidth at millimeter-wave (mmWave) frequencies are underway in communications and sensing [19] to develop short-range technologies. To compensate for the well-known severity of signal power loss due to propagation, large-scale antenna arrays are being employed. Analog–digital hybrid processing schemes have been consequently investigated to minimize the implementation cost and complexity [25]. In this context, reconfigurable holographic surface (RHS) [26] has been proposed recently to realize such large arrays with hybrid processing.

Different from RIS, the RHS is embedded with a large number of meta-material radiation elements connected to an RF chain and is typically integrated with the transceivers; this leads to compact and lightweight transceiver hardware [27], [28]. The low-cost beam maneuverability using amplitude-control was first proposed for the conventional antenna under orthogonal frequency-division-multiplexing (OFDM) transmissions in [29]; it was subsequently extended to the holographic scenario for swift radiation beam control in [30]. The radiation elements of RHS exploit the holographic interference principle [31] to control the *radiation amplitude* of the output radio waves. Recently, RHS has been fabricated with the simple diode-based structure of material leading to lower power consumption and hardware price, with increased flexibility and a swifter beam steering compared to a conventional phased array (PA) [32].

Initial investigations of RHS for flexible beam steering were limited to wireless communications [33], [34]. Recently, RHS-based DFRC has been proposed [35], wherein the holographic beam is aligned toward the LoS target while ensuring a certain required signal-to-interference-plus-noise ratio (SINR) for communication users. However, in dense urban environments, RHS-aided systems, with even improved beam control, yield poor performance in the absence of a stable LoS path. This warranted the use of RIS in a holographic DFRC system [36], [37]. Another noticeable aspect is that the prior-art largely focused on RIS-assisted RF solutions for narrowband signaling thereby leading to simpler frequency-independent passive beamformers. However, future RF systems, sensing and/ or communications, are required to exploit large bandwidths available at the higher frequencies to meet their emerging requirements [19]. Narrowband beamforming techniques offer subpar performance in a wideband setting, where effects like beam squint [25] cannot be ignored.

To overcome the aforementioned limitations, this article explores A wideband DFRC system with the BS transmitter and BS receiver equipped with an RHS and an multiple-input multiple-output (MIMO) array, respectively, while the passive RIS is employed as a reflector [38]. The design variables then comprises the digital beamformer for exploiting the multiple antennas, the holographic beamformer for RHS and the passive beamformer for RIS. These are designed jointly to maximize the radar SINR over all the targets (worst case), while ensuring a certain minimum SINR for the different communication entities. The involves solving a challenging quadratic constraint quartic programming problem with five coupled variables. The proposed solution involves decoupling the original problem into several subproblems which are then solved in an alternating optimization (AO) paradigm. The contributions of this article over prior art are listed as follows.

1) *Wideband RHS Transmission Model:* Different from previous works focused on narrowband RHS-assisted DFRC systems [35], we propose the comprehensive wideband RHS model with OFDM signaling. Our proposed model allows for varying the digital beamforming on different subcarriers, thereby offsetting the beam-squint effect at the transmission end. Previous works have addressed beam squint only in the fully passive RIS [38]. Further, radiation amplitude of the signal input to RHS is controlled to flexibly adjust the resulting beam.
2) *RIS-Aided DFRC With RHS:* Contrary to prior works, we consider simultaneously harnessing the benefits of both RIS and RHS for DFRC applications. This joint deployment is particularly helpful in dense environments, where the channel does not have a stable LoS path between BS and users and/ or targets. Here, the RIS beamforming in the NLoS paths boosts the indirect echoes. Further, RHS transmitters have a small form factor and are able to quickly shape the radiation beampattern to overcome the fast fading channel. However, this deployment scheme imposes a challenge for jointly designing the passive and holographic beamformers.
3) *Joint Digital, Holographic, and Passive Beamformer Design:* Following the system evolution and toward exploiting all the degrees of freedom, we consider a joint design of beamformers—digital, holographic (RHS), and passive (RIS)—and the receive filter to maximize the worst-case radar SINR accounting for all the targets while guaranteeing the communications SINR. This leads to a challenging multivariable max-min nonconvex optimization problem. Toward solving this problem, an AO framework comprising the following steps is then derived: 1) the generalized Rayleigh quotient (GRQ) method to derive the receive filter in a close form; 2) a combined Dinkelbach and majorization–maximization (MM) algorithm to design the digital and holographic beamformers; and 3) the approach based on the Riemannian steepest decent (RSD) [39] and the consensus alternating direction of multipliers (C-ADMM) [40] to address the RIS passive beamforming problem.
4) *Design Outcomes Through Extensive Performance Evaluation:* The undertaken analyses and numerical

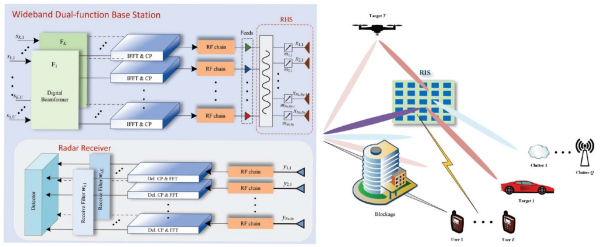

Fig. 1. Illustration of RIS-aided wideband holographic DFRC system.

implementation of the proposed system corroborate the need for both RHS and RIS and illustrate the superior performance of the proposed algorithm in terms of the minimum radar SINR compared with the non-RIS, random-RIS, and random-RHS DFRC systems. Further, the extensive evaluation also depicts a performance tradeoff between communications and radar.

Preliminary ideas from this article were reported in our conference article [1], where we had introduced the wideband RIS-assisted DFRC with RHS, but had restricted the study to a single target. Further, the detailed performance analysis was missing. In this work, we consider a general multitarget scenario which impacts the design procedure. In addition, a critical numerical performance assessment is undertaken to explore different settings and report on the operational benefits.

The rest of this article is organized as follows. Section II introduces the signal model for a RIS-aided wideband DFRC system with RHS and formulates the design problem as an optimization. Section III develops the proposed AO-based algorithm to convert the formulated nonconvex max-min problem into a series of subproblems which are then solved iteratively. Section IV provides extensive numerical simulation examples covering multiple scenarios and benchmarks the gains. Finally, Section V concludes this article.

Notations: Throughout this article, lowercase and uppercase boldface letters represent vectors and matrices, respectively. The classical operations and notations include Transposition $(\cdot)^T$, complex conjugation $(\cdot)^*$, Hermitian $(\cdot)^H$, matrix vectorization vec$(\cdot)$, a diagonal matrix diag$(\cdot)$, and a block diagonal matrix blkdiag$(\cdot)$. The other operators include, the Kronecker product $\otimes$, scalar magnitude $|\cdot|$, ℓ_p norms $\|\cdot\|_p$, and Frobenius norm $\|\cdot\|_F$. Further, $\mathbf{I}_L$ is the $L \times L$ identity matrix and $\mathbf{1}_L$ denotes an L length column vector of ones. $\langle \mathbf{a} \rangle$ denotes a diagonal matrix with diagonal entries derived from the vector $\mathbf{a}$, $\preceq$ denotes the componentwise inequality for vector comparison and $(\cdot)^{(l)}$ denotes the value of a variable at the lth (outer) iteration. The particular notation $|\mathbf{a}| = 1$ means that the absolute value of all elements of vector $\mathbf{a}$ is equal to one.

II. SYSTEM MODEL AND PROBLEM FORMULATION

Consider an RIS-assisted wideband holographic DFRC system (Fig. 1) employing the OFDM signaling with K subcarriers. The far-field coverage area comprises T radar targets, Q clutter patches, and U downlink users in a 3-D Cartesian coordinate system. The dual-function BS (DFBS) is equipped with an RHS fed by N_{RF} RF chains for the transmitter (Tx) and an MIMO array for the radar receiver (Rx).[1]

A. Parameter Definitions

1) *Location Vectors and Relative Angles:* We denote the 3-D position vectors of RIS, the tth target, DFBS, the qth clutter, and the u-th user, respectively, by

$$\mathbf{p}_R = [x_R, y_R, z_R],\ \mathbf{p}_T(t) = [x_T(t), y_T(t), z_T(t)] \quad (1a)$$

$$\mathbf{p}_B = [x_B, y_B, z_B],\ \mathbf{p}_C(q) = [x_C(q), y_C(q), z_C(q)] \quad (1b)$$

$$\mathbf{p}_U(u) = [x_U(u), y_U(u), z_U(u)]. \quad (1c)$$

Further, denote θ_{BR}, θ_{Bu}, θ_{Bt}, and θ_{Bq} as the azimuth angles from DFBS to the RIS, uth user, tth target, and qth clutter, respectively (ψ_{BR}, ψ_{Bu}, ψ_{Bt}, and ψ_{Bq} for elevation). Further, designate the azimuth angles from the RIS to DFBS, uth user, tth target, and qth clutter by θ_{RB}, θ_{Ru}, θ_{Rt}, and θ_{Rq}, respectively (ψ_{RB}, ψ_{Ru}, ψ_{Rt}, and ψ_{Rq} for elevation). Similarly, θ_{uB}, and θ_{uR} are the azimuth angles from the uth user to DFBS, and RIS, respectively (ψ_{uB}, and ψ_{uR} for elevation).

2) *2-D Steering Vectors:* The RHS, (respectively, MIMO array, RIS, user) is equipped with a uniform planar array (UPA) deploying N_x^{Tx} (N_x^{Rx}, N_x^R, N_x^U) and N_y^{Tx} (N_y^{Rx}, N_y^R, N_y^U) antenna elements with an interelement spacing of d_x^{Tx} (d_x^{Rx}, d_x^R, d_x^U) and d_y^{Tx} (d_y^{Rx}, d_y^R, d_y^U) along the x- and y-axes, respectively. The resulting wideband space-frequency steering vectors of RIS, user, DFBS(Tx), and DFBS(Rx) are, respectively,

$$\mathbf{a}_R(f_k, \theta, \psi) = \left[\mathbf{a}_R^x(f_k, \theta, \psi) \otimes \mathbf{a}_R^y(f_k, \theta, \psi)\right] \quad (2a)$$

$$\mathbf{a}_U(f_k, \theta, \psi) = \left[\mathbf{a}_U^x(f_k, \theta, \psi) \otimes \mathbf{a}_U^y(f_k, \theta, \psi)\right] \quad (2b)$$

$$\mathbf{a}_{\text{Tx}}(f_k, \theta, \psi) = \left[\mathbf{a}_{\text{Tx}}^x(f_k, \theta, \psi) \otimes \mathbf{a}_{\text{Tx}}^y(f_k, \theta, \psi)\right] \quad (2c)$$

$$\mathbf{a}_{\text{Rx}}(f_k, \theta, \psi) = \left[\mathbf{a}_{\text{Rx}}^x(f_k, \theta, \psi) \otimes \mathbf{a}_{\text{Rx}}^y(f_k, \theta, \psi)\right] \quad (2d)$$

where $\theta \in [-\pi, \pi]$ ($\psi \in [0, \frac{\pi}{2}]$) are azimuth (elevation) angles, $\lambda_k = c/f_k$ and $f_k = f_c + \hat{f}_k$ are, respectively, the wavelength and frequency of the k subcarrier, f_c and $\hat{f}_k = k\triangle f$ are the carrier frequency and the kth subcarrier offset frequency, respectively, $\triangle f$ is the subcarrier spacing, c is the speed of light, and $\mathbf{a}_l^x(f_k, \theta, \psi)$ ($\mathbf{a}_l^y(f_k, \theta, \psi)$) denote the steering vectors along the x- (y-) axis as

$$\mathbf{a}_l^x(f_k, \theta, \psi) = \left[1, e^{-j\frac{2\pi}{\lambda_k}\mu_x^l}, \ldots, e^{-j\frac{2\pi}{\lambda_k}(N_x^l-1)\mu_x^l}\right]^T \quad (3a)$$

$$\mathbf{a}_l^y(f_k, \theta, \psi) = \left[1, e^{-j\frac{2\pi}{\lambda_k}\mu_y^l}, \ldots, e^{-j\frac{2\pi}{\lambda_k}(N_y^l-1)\mu_y^l}\right]^T \quad (3b)$$

[1]The use of an MIMO array for radar is motivated by the reason to avoid full-duplex operation of the RHS, and thus, simplify the system operations. Herein, we assume that RHS and MIMO array are deployed in the vicinity and hence the direction (i.e., azimuth and elevation) of the target is assumed the same for both RHS and MIMO array.

where $l \in \{R, U, \text{Tx}, \text{Rx}\}$, $\mu_x = d_x \cos\theta \cos\psi$, and $\mu_y = d_y \sin\theta \cos\psi$ are the direction cosines [41]. To simply the notation, hereafter, we denote $N_{\text{Tx}} = N_x^{\text{Tx}} \times N_y^{\text{Tx}}$, $N_{\text{Rx}} = N_x^{\text{Rx}} \times N_y^{\text{Rx}}$, $N_R = N_x^R \times N_y^R$, and $N_U = N_x^U \times N_y^U$ as the total number of array elements in the antennas of the RHS, MIMO array, RIS and communication user.

B. RHS-Based Wideband Transmit Signal

The RHS-based transmitter generates the emitted signal following the holographic interference principle which is first introduced as follows.

1) *Holographic Interference Principle:* RHS is usually deployed as a planar array of the discrete, voltage-tunable meta-atoms with an interelement spacing smaller than $\lambda/2$, i.e., typically $\lambda/4 \sim \lambda/6$. RHS is a leaky-wave antenna that comprises three layers, i.e., N_{RF} feeds connect with the corresponding RF chain embedded in the lowest layer, the waveguide structure installed in the middle layer is used to guide the reference wave to the N_{Tx} discrete subwavelength metamaterial elements integrated on the top layer [30]. At the n_{Tx}th radiation element with the position $[n_x^{\text{Tx}}, n_y^{\text{Tx}}]$, the reference wave imported from the n_{RF}th feed and the object wave (i.e., desired wave) toward a direction of (θ_0, ψ_0) are, respectively, [33], [42]

$$\Psi_{\text{ref}}(n_{\text{RF}}, n_{\text{Tx}}) = e^{-\text{j}\frac{2\pi f}{c}\gamma D_{n_{\text{RF}}, n_{\text{Tx}}}} \tag{4a}$$

$$\Psi_{\text{obj}}(n_{\text{Tx}}, \theta_0, \psi_0) = e^{-\text{j}\frac{2\pi f}{c}((n_x^{\text{Tx}}-1)d_x^B \cos\theta_0 \cos\psi_0 + (n_y^{\text{Tx}}-1)d_y^B \sin\theta_0 \cos\psi_0)} \tag{4b}$$

where γ is the refractive index of the RHS material, $D_{n_{\text{RF}}, n_{\text{Tx}}}$ denotes the distance between the n_{RF}th RF chain and the n_{Tx}th element. Note that herein, for simplicity, the objective wave in (4b) is chosen exactly as the steering vector in the direction (θ_0, ψ_0). Then, the interference between the reference wave and the object wave (i.e., holographic pattern) is defined as

$$\Psi_{\text{intf}}(n_{\text{RF}}, n_{\text{Tx}}, \theta_0, \psi_0) = \Psi_{\text{obj}}(n_{\text{Tx}}, \theta_0, \psi_0)\Psi_{\text{ref}}^*(n_{\text{RF}}, n_{\text{Tx}}). \tag{5}$$

Note that, instead of directly controlling the object wave, RHS can only synthesize the holographic pattern in (5) with the fixed reference wave in (4a). When the holographic pattern is excited by the reference wave, we have [28]

$$\Psi_{\text{intf}}(n_{\text{RF}}, n_{\text{Tx}}, \theta_0, \psi_0)\Psi_{\text{ref}}(n_{\text{RF}}, n_{\text{Tx}}) \propto \Psi_{\text{obj}}(n_{\text{Tx}}, \theta_0, \psi_0)|\Psi_{\text{ref}}(n_{\text{RF}}, n_{\text{Tx}})|^2. \tag{6}$$

Thus, the desired wave toward the direction (θ_0, ψ_0) is generated via controlling the interference in (5). Further, it is evident from (5) and (6) that the interference wave generation requires phase adaption. However, compared with the conventional PA, each element of RHS can only adjust the radiation amplitude of the reference wave.

To illustrate the use of the real-value amplitude of RHS to generate the holographic pattern and hence approximate the desired beam, define the phase of the reference wave in (4a) and the object wave in (4b) as δ_{ref} and δ_{obj}, where the $n_{\text{RF}}, n_{\text{Tx}}, \theta_0, \psi_0$ are omitted for simplifying the notations

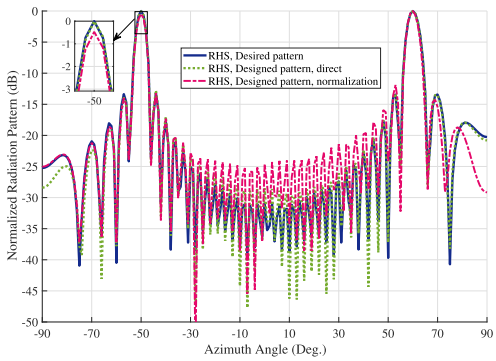

Fig. 2. Comparison of the 2-D desired radiation pattern and the designed pattern of RHS with two desired directions, $\theta_1 = 60^\circ$ and $\theta_2 = -50^\circ$, $d_x^{\text{Tx}} = \frac{\lambda}{6}$, $N_{\text{RF}} = 1$, and $N_{\text{Tx}} = 120$ elements.

and m denotes the amplitude of the corresponding element. Then, we want to achieve the following approximation: $m(\cos(\delta_{\text{ref}}) + j\sin(\delta_{\text{ref}})) \to \cos(\delta_{\text{obj}}) + j\sin(\delta_{\text{obj}})$. This is equivalent to solving the following least squares (LS) problem:

$$\underset{m}{\text{maximize}} \; |\cos(\delta_{\text{obj}}) - m\cos(\delta_{\text{ref}})|^2 + |\sin(\delta_{\text{obj}}) - m\sin(\delta_{\text{ref}})|^2 \tag{7}$$

where the optimal solution is obtained readily as

$$m^\star = \cos(\delta_{\text{obj}} - \delta_{\text{ref}}) = \Re(\Psi_{\text{intf}}). \tag{8}$$

It is seen that the optimal solution of (7) is exactly the real part of the interference. Thus, $\Re(\Psi_{\text{intf}})$ can be used to represent the amplitude of each element to form the beam toward the desired direction. Because the amplitude control is implemented by tuning the dc voltage, we can normalize it to a positive scale as (while accepting some nominal performance loss compared with $\Re(\Psi_{\text{intf}})$) [42]

$$m_{n_{\text{Tx}}}^\star(n_{\text{RF}}, n_{\text{Tx}}, \theta_0, \psi_0) = \frac{\Re(\Psi_{\text{intf}}(n_{\text{RF}}, n_{\text{Tx}}, \theta_0, \psi_0)) + 1}{2} \quad \forall n_{\text{Tx}}. \tag{9}$$

According to (9), it observed that the elements whose reference waves closely match the object wave, i.e., large amplitude, are tuned to emit strongly, otherwise, the radiation elements are tuned down, or even tuned off. Then, for the multibeam design of the holographic pattern, the amplitude of each element is [42]

$$m_{n_{\text{Tx}}}^\star = \sum_{n_{\text{RF}}=1}^{N_{\text{RF}}} \sum_{l=1}^{L} a_{n_{\text{RF}},l} m_{n_{\text{Tx}}}^\star(n_{\text{RF}}, n_{\text{Tx}}, \theta_l, \psi_l), \quad \forall n_{\text{Tx}}. \tag{10}$$

where L denotes the number of the desired direction and $a_{n_{\text{RF}},l}$ denotes the amplitude ratio for the beam toward to the lth direction from the n_{RF}th feed, and it should satisfy: $\sum_{n_{\text{RF}}=1}^{N_{\text{RF}}} \sum_{l=1}^{L} a_{n_{\text{RF}},l} = 1$ which also ensures $0 \le m_{n_{\text{Tx}}}^\star \le 1$. Fig. 2 compares the 2-D transmit beampattern of RHS in different scenarios, i.e., desired pattern, designed pattern with direct (8), and designed pattern with normalized (9). It is seen that the normalization of RHS amplitude leads to a higher sidelobe level and around 0.5-dB mainlobe loss, but still matches the desired pattern well.

2) *OFDM Precoding:* We denote the transmit symbol vector at the kth subcarrier by $\mathbf{s}_k = [s_{k,1}, \ldots, s_{k,U}]^T \in \mathbb{C}^{U\times 1}$, with $\mathbb{E}\{\mathbf{s}_k \mathbf{s}_k^H\} = \mathbf{I}_U$. Let $\mathbf{f}_k$ denote the frequency-dependent digital beamformer to enable MU communications and mitigate the beam-squint effect due to wideband beamforming [43]. After the digital beamforming, the frequency-domain signal at the kth subcarrier is

$$\widetilde{\mathbf{x}_T}[f_k] = \mathbf{f}_k \mathbf{s}_k \in \mathbb{C}^{N_{RF}\times 1}, k = 1, \ldots, K. \tag{11}$$

Applying N_{RF} K-point inverse fast Fourier transform (IFFT) to (11) yields the baseband signal

$$\mathbf{x}_T(t) = \sum_{k=1}^{K} \widetilde{\mathbf{x}_T}[f_k] e^{\mathrm{j}2\pi f_k t} = \sum_{k=1}^{K} \mathbf{f}_k \mathbf{s}_k e^{\mathrm{j}2\pi f_k t} \tag{12}$$

where $t \in (0, T_s]$ and T_s denotes the OFDM duration excluding the cyclic prefix (CP). Then, the signal in (12) is fed to an RHS having N_{Tx} discrete antenna elements.[2]

3) *RHS Beamforming:* For the wideband system, according to (4) and (6), the electromagnetic response of the RHS at the kth subcarrier takes the form [33]

$$\mathbf{V}[f_k] = \mathbf{M}\mathbf{V}_k \in \mathbb{C}^{N_{\mathrm{Tx}}\times N_{\mathrm{RF}}} \tag{13}$$

where the diagonal matrix $\mathbf{M} = \mathrm{diag}[m_{1,1}, \ldots, m_{1,N_y^{\mathrm{Tx}}}, \ldots, m_{N_x^{\mathrm{Tx}},1}, \ldots, m_{N_x^{\mathrm{Tx}},N_y^{\mathrm{Tx}}}]$ and $0 \le m_{n_x^{\mathrm{Tx}},n_y^{\mathrm{Tx}}} \le 1$ is the amplitude-control beamformer of the $(n_x^{\mathrm{Tx}}, n_y^{\mathrm{Tx}})$th RHS element. Further, based on (4a) and OFDM transmission, $\mathbf{V}_k(n_{\mathrm{RF}}, n_{\mathrm{Tx}}) = \Psi_{\mathrm{ref}}(n_{\mathrm{RF}}, n_{\mathrm{Tx}}, f_k) = e^{-2j\pi\gamma D_{n_{\mathrm{RF}},n_{\mathrm{Tx}}}/\lambda_k}$ denotes the reference wave propagation delay at the kth subcarrier, where $n_{\mathrm{Tx}} = 1, \ldots, N_{\mathrm{Tx}}$ and $n_{\mathrm{RF}} = 1, \ldots, N_{\mathrm{RF}}$. Consequently, the matrix $\mathbf{V}_k, k = 1, \ldots, K$ is known if the structure of the holographic surface is fixed and the transmit pattern can be well controlled via tuning the amplitude matrix $\mathbf{M}$.

4) *DFBS Transmit Signal:* After applying the holographic beamforming to (12), the transmitted signal in baseband (excluding CP) takes the form

$$\mathbf{x}(t) = \mathbf{M} \sum_{k=1}^{K} \mathbf{V}_k \mathbf{f}_k \mathbf{s}_k e^{\mathrm{j}2\pi f_k t}. \tag{14}$$

This signal is utilized to simultaneously detect the targets and enable MU communications. Meanwhile, for the DFRC system, the transmit power should meet the system requirement. In general, power constraints for wideband holographic DFRC could be transmit power constraint per subcarrier [33] or total transmit power of all subcarriers [44]. In this article, to fully utilize the bandwidth, we consider the former constraint, i.e.,

$$\|\mathbf{f}_k\|_F^2 \le \mathcal{P}_k \tag{15}$$

where $\mathcal{P}_k$ is the maximum power allocated to the kth subcarrier.

C. Communications Receiver

Denote the direct DFBS(Tx)-user, RIS-user, and DFBS(Tx)-RIS (in which only the LoS component is considered[3]) channels at the kth subcarrier frequency by $\mathbf{H}_{C_u,k}^{\mathrm{dir}}$, $\mathbf{H}_{C_u,k}^{\mathrm{RIS}}$, and $\mathbf{G}_{\mathrm{Tx},k}$, respectively. Following the prevalent Rician channel model summarized in [22] and [46], the aforementioned wideband channel components are, respectively,

$$\mathbf{H}_{C_u,k}^{\mathrm{dir}} = \sqrt{\frac{\Upsilon_{C_u}^{\mathrm{dir}}}{1+\Upsilon_{C_u}^{\mathrm{dir}}}} g_{Bu,k}^{\mathrm{LoS}} \mathbf{a}_U(f_k, \theta_{uB}, \psi_{uB}) \mathbf{a}_{\mathrm{Tx}}^T(f_k, \theta_{Bu}, \psi_{Bu}) + \sqrt{\frac{1}{1+\Upsilon_{C_u,k}^{\mathrm{dir}}}} g_{Bu,k}^{\mathrm{NLoS}} \mathbf{H}_{C_u,k}^{\mathrm{dir,NLoS}} \tag{16a}$$

$$\mathbf{H}_{C_u,k}^{\mathrm{RIS}} = \sqrt{\frac{\Upsilon_{C_u}^{\mathrm{RIS}}}{1+\Upsilon_{C_u}^{\mathrm{RIS}}}} g_{Ru,k}^{\mathrm{LoS}} \mathbf{a}_U(f_k, \theta_{uR}, \psi_{uR}) \mathbf{a}_R^T(f_k, \theta_{Ru}, \psi_{Ru}) + \sqrt{\frac{1}{1+\Upsilon_{C_u}^{\mathrm{RIS}}}} g_{Ru,k}^{\mathrm{NLoS}} \mathbf{H}_{C_u,k}^{\mathrm{RIS,NLoS}} \tag{16b}$$

$$\mathbf{G}_{\mathrm{Tx},k} \approx g_{BR,k}^{\mathrm{LoS}} \mathbf{a}_R(f_k, \theta_{\mathrm{RB}}, \psi_{\mathrm{RB}}) \mathbf{a}_{\mathrm{Tx}}^T(f_k, \theta_{TxR}, \psi_{TxR}), \tag{16c}$$

where $\mathbf{H}_{C_u,k}^{\mathrm{dir,NLoS}}$ and $\mathbf{H}_{C_u,k}^{\mathrm{RIS,NLoS}}$ denote the small-scale NLoS component of the DFBS(Tx)-user and RIS-user links, respectively, with each entry being a circularly symmetric complex Gaussian (CSCG) random variable with zero mean and unit variance [46], $\Upsilon_{C_u}^{\mathrm{dir}}$ and $\Upsilon_{C_u}^{\mathrm{RIS}}$ denote the Rician factors of the corresponding channel, and the path losses for the LoS and NLoS component are modeled as [38], [47]

$$g_{*,k} = \begin{cases} g_{*,k}^{\mathrm{LoS}} = \sqrt{K_{\mathrm{LoS}}(\frac{r_0}{r_*})^{\epsilon_{*,\mathrm{LoS}}}} \\ g_{*,k}^{\mathrm{NLoS}} = \sqrt{K_{\mathrm{NLoS}}(\frac{r_0}{r_*})^{\epsilon_{*,\mathrm{NLoS}}}} \end{cases} \tag{17}$$

where $* \in \{B_u, R_u\}$, r_* denotes the distance of the corresponding path, K_{LoS} (K_{NLoS}) is the path loss at the reference distance r_0 for LoS (NLoS), and $\epsilon_{*,\mathrm{LoS}}$ ($\epsilon_{*,\mathrm{NLoS}}$) is the LoS (NLoS) path loss exponent, which, in practice, is obtained from field tests [47]. To simplify the design procedure, the aforementioned channels are estimated a priori [48], [49], [50]. Thus, our proposed method is not constrained to a specific form (geometric or Rayleigh) of the channel model.

Subsequent to baseband conversion, CP removal, and N_U K-point FFT, the received signal of the uth user on the kth subcarrier is

$$\begin{aligned} \mathbf{y}_{C_u}[f_k] &= \mathbf{H}_{C_u,k}\mathbf{M}\mathbf{V}_k\mathbf{f}_k\mathbf{s}_k + \mathbf{n}_{C_u}[f_k] \\ &= (\mathbf{H}_{C_u,k}^{\mathrm{dir}} + \mathbf{H}_{C_u,k}^{\mathrm{RIS}} \mathbf{\Phi} \mathbf{G}_{\mathrm{Tx},k}) \mathbf{M}\mathbf{V}_k\mathbf{f}_k\mathbf{s}_k + \mathbf{n}_{C_u}[f_k] \end{aligned} \tag{18}$$

where $\mathbf{H}_{C_u,k}$ denotes the composite channel between DFBS(Tx) and the uth user, $\mathbf{\Phi}$ denotes the phase-shift matrix which is common across all subcarriers, $\mathbf{n}_{C_u}[f_k]$ denotes the

[2]Note that the number of feeds should be greater or equal to the number of active data symbols in order to guarantee the decoder performance but less than the number of RHS element to reduce the hardware cost, i.e., $U \le N_{\mathrm{RF}} \le N_{\mathrm{Tx}}$.

[3]In practice, with the exact location of the BS, RIS can be properly installed within sight of the BS. Since the power of NLoS paths is negligible compared to that of the LoS path due to the large Rician factor, the BS-RIS channel can be well approximated by the LoS component [45].

zero-mean white Gaussian noise with covariance $\sigma_c^2\mathbf{I}$ at the receiver front end for the kth subcarrier.

REMARK 1 Frequency Independent RIS operation: Due to the passive nature of RIS which precludes baseband signal processing unit, RIS can only work in the resonance frequency, and thus, the phase-shift is common for all subcarriers [51], [52], [53]. Hence, the beam-squint effect which degrades the performance of the wideband system is also inevitable at RIS. While there exist some works aiming to design subcarrier-specific phase shifts to overcome the squint [38], the complexity of their hardware implementation is beyond the envisaged DFRC system [54]. Hence, in this article, we consider the fully passive RIS-assisted wideband DFRC with RHS.

At the kth subcarrier of the uth user, a digital combiner $\mathbf{w}_{k,u}$ is utilized to filter the received signal and estimate the transmitted symbol as

$$\tilde{s}_{k,u} = \mathbf{w}_{k,u}^H \mathbf{H}_{C_u,k}\mathbf{M}\mathbf{V}_k\mathbf{f}_{k,u}s_{k,u} + \sum_{i\neq u}^{U} \mathbf{w}_{k,u}^H \mathbf{H}_{C_u,k}\mathbf{M}\mathbf{V}_k\mathbf{f}_{k,i}s_{k,i} + \mathbf{w}_{k,u}^H \mathbf{n}_{C_u}[f_k]. \tag{19}$$

Because the quality of the estimate $s_{k,u}$ is determined by the SINR, it is the typical metric for benchmarking the link performance of communication. According to (19), the SINR of the uth user on the kth subcarrier is

$$\mathrm{SINR}_{C_u,k} = \frac{\|\mathbf{w}_{k,u}^H \mathbf{H}_{C_u,k}\mathbf{M}\mathbf{V}_k\mathbf{f}_k\mathbf{\Lambda}_u\|^2}{\|\mathbf{w}_{k,u}^H \mathbf{H}_{C_u,k}\mathbf{M}\mathbf{V}_k\mathbf{f}_k\widetilde{\mathbf{\Lambda}}_u\|^2 + \sigma_c^2\mathbf{w}_{k,u}^H\mathbf{w}_{k,u}} \tag{20}$$

where $\mathbf{\Lambda}_u \in \mathbb{R}^{U\times U}$ is the diagonal matrix with the uth diagonal element is one and the others are zero and $\widetilde{\mathbf{\Lambda}}_u = \mathbf{I}_U - \mathbf{\Lambda}_u$.

D. Radar Receiver

The signal at the radar receiver follows a model similar to that of communications with the addition of a two-way propagation. Similar to Section II-C, after sampling, CP removal and applying N_{Rx} K-point FFT, the echo signal on the kth subcarrier at the radar receiver is

$$\mathbf{y}_R[f_k] = \sum_{t=1}^{T} \mathbf{H}_{R_t,k}\mathbf{M}\mathbf{V}_k\mathbf{f}_k\mathbf{s}_k + \sum_{q=1}^{Q} \mathbf{H}_{R_q,k}\mathbf{M}\mathbf{V}_k\mathbf{f}_k\mathbf{s}_k + \mathbf{n}_R[f_k] \tag{21}$$

where the composite channels across the DFBS-tth target receiver and the DFBS-qth clutter-receiver are, respectively,

$$\mathbf{H}_{R_t,k} = \alpha_t(\mathbf{h}_{\mathrm{Rx},k,t}^T + \mathbf{G}_{\mathrm{Rx},k}^T\mathbf{\Phi}\mathbf{b}_{k,t}^T)(\mathbf{h}_{\mathrm{Tx},k,t} + \mathbf{b}_{k,t}\mathbf{\Phi}\mathbf{G}_{\mathrm{Tx},k}) \tag{22a}$$

$$\mathbf{H}_{R_q,k} = \alpha_q(\mathbf{h}_{\mathrm{Rx},k,q}^T + \mathbf{G}_{\mathrm{Rx},k}^T\mathbf{\Phi}\mathbf{b}_{k,q}^T)(\mathbf{h}_{\mathrm{Tx},k,q} + \mathbf{b}_{k,q}\mathbf{\Phi}\mathbf{G}_{\mathrm{Tx},k}) \tag{22b}$$

where α_t and α_q denote the RCS for the tth target and the qth clutter, respectively, $\mathbf{h}_{\mathrm{Tx},k,t} = g_{Bt,k}\mathbf{a}_{\mathrm{Tx}}^T(f_k,\theta_{Bt},\psi_{Bt})$ denotes the channel from DFBS(Tx) to target, $\mathbf{h}_{\mathrm{Rx},k,t} = g_{Bt,k}\mathbf{a}_{\mathrm{Rx}}^T(f_k,\theta_{Bt},\psi_{Bt})$ denotes the channel from DFBS(Rx) to target, $\mathbf{b}_{k,t} = g_{Rt,k}\mathbf{a}_R^T(f_k,\theta_{Rt},\psi_{Rt})$ denotes the path from RIS to target, in which

$$g_{Bt,k} = \sqrt{K_{Bt}\left(\frac{r_0}{\|\mathbf{p}_B - \mathbf{p}_T(t)\|_2}\right)^{\epsilon_{Bt}}} \tag{23a}$$

$$g_{Rt,k} = \sqrt{K_{Rt}\left(\frac{r_0}{\|\mathbf{p}_R - \mathbf{p}_T(t)\|_2}\right)^{\epsilon_{Rt}}} \tag{23b}$$

denote the free-space path loss with the path-loss exponent ϵ_{Bt} and ϵ_{Rt}, and $\mathbf{G}_{\mathrm{Rx},k}$ denotes the DFBS(Rx)-RIS channel which is similarly defined as (16c) and, hence, omit it herein.

In radar systems, target detection performance primarily hinges on the output SINR,[4] i.e., the detection performance for a given false-alarm improves with the increase of SINR [55]. Consequently, SINR maximization serves as a widely employed optimization criterion [56]. As in the communications system, in the case of multiple targets, the SINR for each of the targets needs to be improved, particularly, improving the echo signal while suppressing interference. However, unlike the communications symbols embedded in each subcarrier, the radar receiver can employ the detector by combining the echo signals from all subcarriers (Fig. 1). In this context, based on (21), define the radar SINR for the tth target as

$$\mathrm{SINR}_{R_t} = \frac{\sum_{k=1}^{K}\|\mathbf{w}_{k,t}^H\mathbf{H}_{R_t,k}\mathbf{M}\mathbf{V}_k\mathbf{f}_k\|_2^2}{\sum_{k=1}^{K}(\sum_{j\neq t}^{T}\sum_{q=1}^{Q}\|\mathbf{w}_{k,t}^H\mathbf{H}_{R_{j,q},k}\mathbf{M}\mathbf{V}_k\mathbf{f}_k\|_2^2 + \sigma_r^2\mathbf{w}_{k,t}^H\mathbf{w}_{k,t})} \tag{24}$$

where $\mathbf{w}_{k,t}$ is the radar receive filter at the k-subcarrier [57].

REMARK 2 Transmit beampattern matching is another approach widely employed as the optimal design criterion for radar sensing in the conventional and RHS-aided DFRC system without RIS [35], [58], [59], [60]. However, this may not be directly applicable for RIS-assisted radar-only or DFRC systems, especially, in dense environments [13], [61] because it is difficult to balance the beam intensity toward the target and RIS directions even with the path-loss information. For example, if the LoS path is totally blocked, then the allocation of power to the direct link is not needed. Further, in such environments with a weak or no LoS channel, aggregated interference caused by multiple reflections from other objects in the environment could result in performance loss, despite the beampattern design. Hence, the output SINR, which includes these artifacts and the design of the received filter, is recognized as the proper radar metric for RIS-aided DFRC [62], [63].

[4]Herein, interference includes clutter response in addition to the response from other targets.

E. Problem Formulation

In this article, we consider the radar-centric DFRC which maximizes the worst-case radar SINR while guaranteeing the communications SINR over all subcarriers and users. Based on the above, we formulate this optimization problem as

$$\underset{\mathbf{w}_{k,t},\mathbf{w}_{k,u},\mathbf{f}_k,\mathbf{\Phi},\mathbf{M}}{\text{maximize}} \quad \min_t \text{SINR}_{R_t} \tag{25a}$$

$$\text{subject to} \quad |\mathbf{\Phi}| = 1 \tag{25b}$$

$$\text{SINR}_{C_u,k} \geq \eta \quad \forall u \quad \forall k \tag{25c}$$

$$0 \leq m_{n_x^{\text{Tx}},n_y^{\text{Tx}}} \leq 1 \tag{25d}$$

$$\|\mathbf{f}_k\|_F^2 \leq \mathcal{P}_k \tag{25e}$$

where $|\mathbf{\Phi}| = 1$ indicates unit magnitude for each diagonal entry of the phase-matrix $\mathbf{\Phi}$, $m_{n_x,n_y} = 0$ denotes that the (n_x, n_y)th RHS element is disabled and $m_{n_x,n_y} = 1$ denotes that the (n_x, n_y)th RHS element is unit gain, and (25c) denotes the fairness SINR constraint over different users and subcarriers, in which η denotes the threshold of communications SINR. Note that the above optimization problem involves the maximin objective function, difference of convex (DC), and unimodular constraints. Meanwhile, it is a fractional quadratically constrained quartic program (QCQP) problem in multiple variables, and thus, difficult to solve directly. Despite the existence of several approaches for nonlinear optimization addressing fractional QCQP for a single variable, the problem in (25) poses unique challenges that prevent an adaptation of using existing methods. These challenges include, highly coupled variables, maximin objective and several nonconvex constraints as well as presence of discrete variables. As a consequence, we develop the AO algorithm in the sequel.

III. ALTERNATING OPTIMIZATION

We first decouple the nonconvex fractional QCQP into four subproblems of designing the receive filter along with digital, holographic, and passive beamformers. Then, we resort to the AO procedure to solve these problems iteratively.

A. Subproblem 1: Update of Receive Filter

We first define the radar filter $\mathbf{w}_t = [\mathbf{w}_{1,t}^T, \ldots, \mathbf{w}_{K,t}^T]^T$ for all subcarriers. Then, for fixed $\mathbf{\Phi}$, $\mathbf{f}_k$ and $\mathbf{M}$, the subproblem with respect to $\mathbf{w}_{k,t}$ and $\mathbf{w}_{k,u}$ is

$$\mathcal{P}_1 \begin{cases} \underset{\mathbf{w}_t,\mathbf{w}_u}{\text{maximize}} \ \min_t \frac{\mathbf{w}_t^H \mathbf{\Sigma}_t^{\mathcal{P}_1} \mathbf{w}_t}{\mathbf{w}_t^H \widetilde{\mathbf{\Sigma}}_t^{\mathcal{P}_1} \mathbf{w}_t + \sigma_r^2 \mathbf{w}_t^H \mathbf{w}_t} \\ \text{subject to} \ \frac{\mathbf{w}_{k,u}^H \mathbf{\Sigma}_{k,u}^{\mathcal{P}_1} \mathbf{w}_{k,u}}{\mathbf{w}_{k,u}^H \widetilde{\mathbf{\Sigma}}_{k,u}^{\mathcal{P}_1} \mathbf{w}_{k,u} + \sigma_c^2 \mathbf{w}_{k,u}^H \mathbf{w}_{k,u}} \geq \eta \quad \forall k \quad \forall u, \end{cases} \tag{26}$$

where the block diagonal matrix used in $\mathcal{P}_1$ is given by

$$\mathbf{\Sigma}_t^{\mathcal{P}_1} = \text{blkdiag}[\mathbf{\Sigma}_{1,t}^{\mathcal{P}_1}, \ldots, \mathbf{\Sigma}_{K,t}^{\mathcal{P}_1}], \ t = 1, \ldots, T \tag{27}$$

$$\widetilde{\mathbf{\Sigma}}_t^{\mathcal{P}_1} = \text{blkdiag}[\widetilde{\mathbf{\Sigma}}_{1,t}^{\mathcal{P}_1}, \ldots, \widetilde{\mathbf{\Sigma}}_{K,t}^{\mathcal{P}_1}], \ t = 1, \ldots, T \tag{28}$$

and

$$\mathbf{\Sigma}_{k,u}^{\mathcal{P}_1} = \mathbf{H}_{C_u,k} \mathbf{M} \mathbf{V}_k \mathbf{f}_k \mathbf{\Lambda} \mathbf{f}_k^H \mathbf{V}_k^H \mathbf{M}^H \mathbf{H}_{C_u,k}^H \tag{29a}$$

$$\widetilde{\mathbf{\Sigma}}_{k,u}^{\mathcal{P}_1} = \mathbf{H}_{C_u,k} \mathbf{M} \mathbf{V}_k \mathbf{f}_k \widetilde{\mathbf{\Lambda}} \mathbf{f}_k^H \mathbf{V}_k^H \mathbf{M}^H \mathbf{H}_{C_u,k}^H \tag{29b}$$

$$\mathbf{\Sigma}_{k,t}^{\mathcal{P}_1} = \mathbf{H}_{R_t,k} \mathbf{M} \mathbf{V}_k \mathbf{f}_k \mathbf{f}_k^H \mathbf{V}_k^H \mathbf{M} \mathbf{H}_{R_t,k}^H \tag{29c}$$

$$\widetilde{\mathbf{\Sigma}}_{k,t}^{\mathcal{P}_1} = \sum_{j \neq t}^{T} \sum_{q=1}^{Q} \mathbf{H}_{R_{j,q},k} \mathbf{M} \mathbf{V}_k \mathbf{f}_k \mathbf{f}_k^H \mathbf{V}_k^H \mathbf{M} \mathbf{H}_{R_{j,q},k}^H. \tag{29d}$$

Note that the objective function of problem (26) is separable in terms of the variables $\mathbf{w}_t$ and $\mathbf{w}_{k,u}$. Hence, we obtain an optimal solution for the maximin problem (26) by solving the following disjoint problems:

$$\mathcal{P}_{1.1} \begin{cases} \underset{\mathbf{w}_t}{\text{maximize}} \ \frac{\mathbf{w}_t^H \mathbf{\Sigma}_t^{\mathcal{P}_1} \mathbf{w}_t}{\mathbf{w}_t^H \widetilde{\mathbf{\Sigma}}_t^{\mathcal{P}_1} \mathbf{w}_t + \sigma_r^2 \mathbf{w}_t^H \mathbf{w}_t} \\ \underset{\mathbf{w}_{k,u}}{\text{maximize}} \ \frac{\mathbf{w}_{k,u}^H \mathbf{\Sigma}_{k,u}^{\mathcal{P}_1} \mathbf{w}_{k,u}}{\mathbf{w}_{k,u}^H \widetilde{\mathbf{\Sigma}}_{k,u}^{\mathcal{P}_1} \mathbf{w}_{k,u} + \sigma_c^2 \mathbf{w}_{k,u}^H \mathbf{w}_{k,u}} \end{cases} \tag{30}$$

where $k = 1, \ldots, K, t = 1, \ldots, T$, and $u = 1, \ldots, U$. Note that $\mathcal{P}_{1.1}$ is composed of a set of GRQ programming which can be solved by the following Proposition 1.

PROPOSITION 1 For a fixed Hermitian matrix $\mathbf{A}$, and a fixed positive definite matrix $\mathbf{B}$, the maximum values λ^* of the GRQ $\frac{\mathbf{w}^H \mathbf{A} \mathbf{w}}{\mathbf{w}^H \mathbf{B} \mathbf{w}}$, where $\mathbf{w} \neq \mathbf{0}$ and the corresponding vector $\mathbf{w}^*$ satisfy: $\lambda^* = \lambda_{\max}(\mathbf{B}^{-1}\mathbf{A})$, $\mathbf{w}^* = \rho_{\max}(\mathbf{B}^{-1}\mathbf{A})$, where $\lambda_{\max}(\cdot)$ and $\rho_{\max}(\cdot)$ denotes the operation of largest eigenvalue and principal eigenvector.

PROOF See [64]. ■

Based on Proposition 1, the close-form solution of $\mathcal{P}_{1.1}$ is given by

$$\mathbf{w}_t^* = \rho_{\max}((\widetilde{\mathbf{\Sigma}}_t^{\mathcal{P}_1} + \sigma_r^2 \mathbf{I}_{N_{\text{Tx}}K})^{-1} \mathbf{\Sigma}_t^{\mathcal{P}_1}) \quad \forall t \tag{31a}$$

$$\mathbf{w}_{k,u}^* = \rho_{\max}((\widetilde{\mathbf{\Sigma}}_{k,u}^{\mathcal{P}_1} + \sigma_c^2 \mathbf{I}_{N_U K})^{-1} \mathbf{\Sigma}_{k,u}^{\mathcal{P}_1}) \quad \forall k \quad \forall u. \tag{31b}$$

B. Subproblem 2: Update of Digital Beamformer

For the fixed $\mathbf{w}_{k,t}$, $\mathbf{w}_{k,u}$, $\mathbf{M}$, and $\mathbf{\Phi}$, the subproblem with respect to $\mathbf{f}_k$ is

$$\mathcal{P}_2 \begin{cases} \underset{\mathbf{f}}{\text{maximize}} \ \min_t \frac{\mathbf{f}^H \mathbf{\Sigma}_t^{\mathcal{P}_2} \mathbf{f}}{\mathbf{f}^H \widetilde{\mathbf{\Sigma}}_t^{\mathcal{P}_2} \mathbf{f} + \sigma_r^2 \mathbf{w}_t^H \mathbf{w}_t} \\ \text{subject to} \ \|\mathbf{S}_k \mathbf{f}\|_2^2 \leq \mathcal{P}_k \quad \forall k \\ \frac{\mathbf{f}^H \mathbf{S}_k^H \mathbf{\Sigma}_{k,u}^{\mathcal{P}_2} \mathbf{S}_k \mathbf{f}}{\mathbf{f}^H \mathbf{S}_k^H \widetilde{\mathbf{\Sigma}}_{k,u}^{\mathcal{P}_2} \mathbf{S}_k \mathbf{f} + \sigma_c^2 \mathbf{w}_{k,u}^H \mathbf{w}_{k,u}} \geq \eta \quad \forall k \quad \forall u \end{cases} \tag{32}$$

where $\mathbf{f} = [\text{vec}(\mathbf{f}_1)^T, \ldots, \text{vec}(\mathbf{f}_K)^T]^T$, $\mathbf{S}_k = \mathbf{\Lambda}_k \otimes \mathbf{I}_{N_{\text{RF}}U}$ denotes the selection matrix to extract the kth interval of vector, $\mathbf{\Xi} = \text{blkdiag}[(\mathbf{I}_U \otimes \mathbf{M}\mathbf{V}_1), \ldots, (\mathbf{I}_U \otimes \mathbf{M}\mathbf{V}_K)]$, and the block diagonal matrices $\mathbf{\Sigma}_t^{\mathcal{P}_2}$ and $\widetilde{\mathbf{\Sigma}}_t^{\mathcal{P}_2}$ are, respectively, defined as

$$\mathbf{\Sigma}_t^{\mathcal{P}_2} = \text{blkdiag}[\mathbf{\Sigma}_{1,t}^{\mathcal{P}_2}, \ldots, \mathbf{\Sigma}_{K,t}^{\mathcal{P}_2}], \ t = 1, \ldots, T \tag{33a}$$

$$\widetilde{\mathbf{\Sigma}}_t^{\mathcal{P}_2} = \text{blkdiag}[\widetilde{\mathbf{\Sigma}}_{1,t}^{\mathcal{P}_2}, \ldots, \widetilde{\mathbf{\Sigma}}_{K,t}^{\mathcal{P}_2}], \ t = 1, \ldots, T \tag{33b}$$

and

$$\mathbf{\Sigma}_{k,u}^{\mathcal{P}_2} = \mathbf{\Lambda}_u \otimes \mathbf{V}_k^H \mathbf{M}^H \mathbf{H}_{C_u,k}^H \mathbf{w}_{k,u} \mathbf{w}_{k,u}^H \mathbf{H}_{C_u,k} \mathbf{M} \mathbf{V}_k \tag{34a}$$

$$\widetilde{\mathbf{\Sigma}}_{k,u}^{\mathcal{P}_2} = \widetilde{\mathbf{\Lambda}}_u \otimes \mathbf{V}_k^H \mathbf{M}^H \mathbf{H}_{C_u,k}^H \mathbf{w}_{k,u} \mathbf{w}_{k,u}^H \mathbf{H}_{C_u,k} \mathbf{M} \mathbf{V}_k \tag{34b}$$

$$\mathbf{\Sigma}_{k,t}^{\mathcal{P}_2} = \mathbf{I}_U \otimes \mathbf{V}_k^H \mathbf{M}^H \mathbf{H}_{R_t,k}^H \mathbf{w}_{k,t} \mathbf{w}_{k,t}^H \mathbf{H}_{R_t,k} \mathbf{M} \mathbf{V}_k \tag{34c}$$

$$\widetilde{\mathbf{\Sigma}}_{k,t}^{\mathcal{P}_2} = \mathbf{I}_U \otimes \sum_{j\neq t}^{T}\sum_{q=1}^{Q} \mathbf{V}_k^H \mathbf{M}^H \mathbf{H}_{R_{j,q},k}^H \mathbf{w}_{k,t}\mathbf{w}_{k,t}^H \mathbf{H}_{R_{j,q},k}\mathbf{M}\mathbf{V}_k. \tag{34d}$$

It is worth noting that $\mathcal{P}_2$ is highly nonconvex due to the fractional quadratic objective function and DC constraint. Inspired by the minorization–maximization (MM) algorithm [65], we can linearize the corresponding convex function. Specifically, for the function $f(\mathbf{x}) = \mathbf{x}^H\mathbf{H}\mathbf{x}$, the following inequality is always satisfied:

$$f(\mathbf{x}) \geq 2\Re(\mathbf{x}^{(l)H}\mathbf{H}\mathbf{x}) - f(\mathbf{x}^{(l)}) \tag{35}$$

where $\mathbf{H}$ is positive semidefinite (PSD) matrix, $\mathbf{x}^{(l)}$ denotes the current point (at the lth iteration), and the equality holds if and only if $\mathbf{x} = \mathbf{x}^{(l)}$; see [66].

Based on (35), we simplify $\mathcal{P}_2$ as

$$\mathcal{P}_{2.1}\begin{cases} \text{maximize}_{\mathbf{f}}\ \min_t \frac{2\Re(\mathbf{f}^{(l)H}\mathbf{\Sigma}_t^{\mathcal{P}_2}\mathbf{f}) - \mathbf{f}^{(l)H}\mathbf{\Sigma}_t^{\mathcal{P}_2}\mathbf{f}^{(l)}}{\mathbf{f}^H\widetilde{\mathbf{\Sigma}}_t^{\mathcal{P}_2}\mathbf{f} + \sigma_r^2\mathbf{w}_t^H\mathbf{w}_t} \\ \text{subject to}\quad \|\mathbf{S}_k\mathbf{f}\|_2^2 \leq \mathcal{P}_k \quad \forall k \\ \frac{2\Re(\mathbf{f}^{(l)H}\mathbf{S}_k^H\mathbf{\Sigma}_{k,u}^{\mathcal{P}_2}\mathbf{S}_k\mathbf{f}) - \mathbf{f}^{(l)H}\mathbf{S}_k^H\mathbf{\Sigma}_{k,u}^{\mathcal{P}_2}\mathbf{S}_k\mathbf{f}^{(l)}}{\mathbf{f}^H\mathbf{S}_k^H\widetilde{\mathbf{\Sigma}}_{k,u}^{\mathcal{P}_2}\mathbf{S}_k\mathbf{f} + \sigma_c^2\mathbf{w}_{k,u}^H\mathbf{w}_{k,u}} \geq \eta,\ \forall k,\forall u \end{cases} \tag{36}$$

where $\mathbf{f}^{(l)}$ denotes the value of $\mathbf{f}$ at the lth outer AM iteration. This is a standard fractional maximin problem that can be solved using the generalized Dinkelbach-based method [67]. Thus, we solve problem (36) by reformulating it as

$$\mathcal{P}_{2.2}\begin{cases} \underset{\mathbf{f}}{\text{maximize}}\ \min_t 2\Re(\mathbf{f}^{(l)H}\mathbf{\Sigma}_t^{\mathcal{P}_2}\mathbf{f}) - \lambda_{\mathcal{P}_2}\mathbf{f}^H\widetilde{\mathbf{\Sigma}}_t^{\mathcal{P}_2}\mathbf{f} \\ \text{subject to}\quad \|\mathbf{S}_k\mathbf{f}\|_2^2 \leq \mathcal{P}_k \quad \forall k, \\ \frac{2\Re(\mathbf{f}^{(l)H}\mathbf{S}_k^H\mathbf{\Sigma}_u^{\mathcal{P}_2}\mathbf{S}_k\mathbf{f}) - \mathbf{f}^{(l)H}\mathbf{S}_k^H\mathbf{\Sigma}_u^{\mathcal{P}_2}\mathbf{S}_k\mathbf{f}^{(l)}}{\mathbf{f}^H\mathbf{S}_k^H\widetilde{\mathbf{\Sigma}}_u^{\mathcal{P}_2}\mathbf{S}_k\mathbf{f} + \sigma_c^2\mathbf{w}_{k,u}^H\mathbf{w}_{k,u}} \geq \eta,\ \forall k,\ \forall u, \end{cases} \tag{37}$$

which is equivalently reformulated as

$$\mathcal{P}_{2.3}\begin{cases} \underset{\mathbf{f}}{\text{maximize}}\ \xi_{\mathcal{P}_{2.3}} \\ \text{subject to}\quad \|\mathbf{S}_k\mathbf{f}\|_2^2 \leq \mathcal{P}_k \quad \forall k \\ 2\Re(\mathbf{f}^{(l)H}\mathbf{\Sigma}_t^{\mathcal{P}_2}\mathbf{f}) - \lambda_{\mathcal{P}_2}\mathbf{f}^H\widetilde{\mathbf{\Sigma}}_t^{\mathcal{P}_2}\mathbf{f} \geq \xi_{\mathcal{P}_{2.3}} \quad \forall t \\ \frac{2\Re(\mathbf{f}^{(l)H}\mathbf{S}_k^H\mathbf{\Sigma}_u^{\mathcal{P}_2}\mathbf{S}_k\mathbf{f})\mathbf{f}^{(l)H}\mathbf{S}_k^H\mathbf{\Sigma}_u^{\mathcal{P}_2}\mathbf{S}_k\mathbf{f}^{(l)}}{\mathbf{f}^H\mathbf{S}_k^H\widetilde{\mathbf{\Sigma}}_u^{\mathcal{P}_2}\mathbf{S}_k\mathbf{f} + \sigma_c^2\mathbf{w}_{k,u}^H\mathbf{w}_{k,u}} \geq \eta,\ \forall k,\forall u \end{cases} \tag{38}$$

and hence solved by using Algorithm 1. Noted that for the simplified two variables quadratic programming with convex constraints (37), the Dinkelbach algorithm can be convergent to the global optimal solution [67].

C. Subproblem 3: Update of Holographic Beamformer

With $\mathbf{w}_{k,t}$, $\mathbf{w}_{k,u}$, $\mathbf{f}_k$, and $\mathbf{\Phi}$ fixed, the subproblem with respect to $\mathbf{M}$ is

$$\mathcal{P}_3\begin{cases} \underset{\mathbf{0}\preceq\mathbf{m}\preceq\mathbf{1}}{\text{maximize}}\ \min_t \frac{\mathbf{m}^T\Re(\mathbf{\Sigma}_t^{\mathcal{P}_3})\mathbf{m}}{\mathbf{m}^T\Re(\widetilde{\mathbf{\Sigma}}_t^{\mathcal{P}_3})\mathbf{m} + \sigma_r^2\mathbf{w}_t^H\mathbf{w}_t} \\ \text{subject to}\ \frac{\mathbf{m}^T\Re(\mathbf{\Sigma}_{k,u}^{\mathcal{P}_3})\mathbf{m}}{\mathbf{m}^T\Re(\widetilde{\mathbf{\Sigma}}_{k,u}^{\mathcal{P}_3})\mathbf{m} + \sigma_c^2\mathbf{w}_{k,u}^H\mathbf{w}_{k,u}} \geq \eta,\ \forall k,\forall u \end{cases} \tag{39}$$

where $\mathbf{m} = \mathbf{M}^T\mathbf{1}_{N_xN_y}$ and the matrices $\mathbf{\Sigma}_{k,u}^{\mathcal{P}_3}$, $\widetilde{\mathbf{\Sigma}}_{k,u}^{\mathcal{P}_3}$, $\mathbf{\Sigma}_t^{\mathcal{P}_3}$, and $\widetilde{\mathbf{\Sigma}}_t^{\mathcal{P}_3}$ are similarly defined as

$$\mathbf{\Sigma}_{k,u}^{\mathcal{P}_3} = \langle \mathbf{w}_{k,u}^H\mathbf{H}_{C_u,k}\rangle \mathbf{V}_k\mathbf{f}_k\mathbf{\Lambda}_u\mathbf{f}_k^H\mathbf{V}_k^H\langle \mathbf{w}_{k,u}^T\mathbf{H}_{C_u,k}^*\rangle \tag{40a}$$

$$\widetilde{\mathbf{\Sigma}}_{k,u}^{\mathcal{P}_3} = \langle \mathbf{w}_{k,u}^H\mathbf{H}_{C_u,k}\rangle \mathbf{V}_k\mathbf{f}_k\widetilde{\mathbf{\Lambda}}_u\mathbf{f}_k^H\mathbf{V}_k^H\langle \mathbf{w}_{k,u}^T\mathbf{H}_{C_u,k}^*\rangle \tag{40b}$$

Algorithm 1: Dinkelbach-Based Algorithm to Solve $\mathcal{P}_{2.1}$.

Input: ϵ_1, $\mathbf{f}^{(l)}$, $\mathcal{P}_k$, $\mathbf{S}_k$, $\mathbf{\Xi}$, $\mathbf{\Sigma}_t^{\mathcal{P}_2}$, $\widetilde{\mathbf{\Sigma}}_t^{\mathcal{P}_2}$, $\mathbf{\Sigma}_u^{\mathcal{P}_2}$ and $\widetilde{\mathbf{\Sigma}}_u^{\mathcal{P}_2}$.
Output: $\mathbf{f}^{(l+1)}$

Set $l_2 = 0$, $\mathbf{f}_{l_2} = \mathbf{f}^{(l)}$;
$\lambda_{\mathcal{P}_2}^{(l_2)} = \min_t \frac{2\Re(\mathbf{f}_{l_2}{}^H\mathbf{\Sigma}_t^{\mathcal{P}_2}\mathbf{f}_{l_2}) - \mathbf{f}_{l_2}{}^H\mathbf{\Sigma}_t^{\mathcal{P}_2}\mathbf{f}_{l_2}}{\mathbf{f}_{l_2}^H\widetilde{\mathbf{\Sigma}}_t^{\mathcal{P}_2}\mathbf{f}_{l_2} + \sigma_r^2\mathbf{w}_t^H\mathbf{w}_t}$
repeat
  Find $\mathbf{f}_{l_2}$ by solving problem (38) using $\mathcal{P}_k$, $\mathbf{R}_u$, $\widetilde{\mathbf{R}}_u$, $\mathbf{\Xi}_{p,t}$, and $\mathbf{\Xi}_{p,c}$;
  $F_{\lambda_{\mathcal{P}_2}^{(l_2)}} = \min_t 2\Re(\mathbf{f}^{(l)H}\mathbf{\Sigma}_t^{\mathcal{P}_2}\mathbf{f}_{l_2}) - \lambda_f^{(l_2)}\mathbf{f}_{l_2}^H\widetilde{\mathbf{\Sigma}}_t^{\mathcal{P}_2}\mathbf{f}_{l_2}$;
  $l_2 \leftarrow l_2 + 1$;
  Update $\lambda_{\mathcal{P}_2}^{(l_2)} = \min_t \frac{2\Re(\mathbf{f}^{(l)H}\mathbf{\Sigma}_t^{\mathcal{P}_2}\mathbf{f}_{l_2}) - \mathbf{f}^{(l)H}\mathbf{\Sigma}_t^{\mathcal{P}_2}\mathbf{f}^{(l)}}{\mathbf{f}_{l_2}^H\widetilde{\mathbf{\Sigma}}_t^{\mathcal{P}_2}\mathbf{f}_{l_2} + \sigma_r^2\mathbf{w}_t^H\mathbf{w}_t}$;
until $F_{\lambda_{l_2}} \leq \epsilon_1$ or reach the maximum iteration.
return $\mathbf{f}^{(l+1)} = \mathbf{f}_{l_2}$.

$$\mathbf{\Sigma}_t^{\mathcal{P}_3} = \sum_{k=1}^{K}\langle \mathbf{w}_{k,t}^H\mathbf{H}_{R_t,k}\rangle \mathbf{V}_k\mathbf{f}_k\mathbf{f}_k^H\mathbf{V}_k^H\langle \mathbf{w}_{k,t}^T\mathbf{H}_{R_t,k}^*\rangle \tag{40c}$$

$$\widetilde{\mathbf{\Sigma}}_t^{\mathcal{P}_3} = \sum_{j\neq t}^{T}\sum_{q=1}^{Q}\sum_{k=1}^{K}\langle \mathbf{w}_{k,t}^H\mathbf{H}_{R_{j,q},k}\rangle \mathbf{V}_k\mathbf{f}_k\mathbf{f}_k^H\mathbf{V}_k^H\langle \mathbf{w}_{k,t}^T\mathbf{H}_{R_{j,q},k}^*\rangle. \tag{40d}$$

Similar to $\mathcal{P}_2$, we reformulate $\mathcal{P}_3$ as

$$\mathcal{P}_{3.1}\begin{cases} \underset{\mathbf{0}\preceq\mathbf{m}\preceq\mathbf{1}}{\text{maximize}}\ \min_t \frac{2\mathbf{m}^{(l)T}\Re(\mathbf{\Sigma}_t^{\mathcal{P}_3})\mathbf{m} - \mathbf{m}^{(l)T}\Re(\mathbf{\Sigma}_t^{\mathcal{P}_3})\mathbf{m}^{(l)}}{\mathbf{m}^T\Re(\widetilde{\mathbf{\Sigma}}_t^{\mathcal{P}_3})\mathbf{m} + \sigma_r^2\mathbf{w}_t^H\mathbf{w}_t} \\ \text{subject to}\ \frac{2\mathbf{m}^{(l)T}\Re(\mathbf{\Sigma}_{k,u}^{\mathcal{P}_3})\mathbf{m} - \mathbf{m}^{(l)T}\Re(\mathbf{\Sigma}_{k,u}^{\mathcal{P}_3})\mathbf{m}^{(l)}}{\mathbf{m}^T\Re(\widetilde{\mathbf{\Sigma}}_{k,u}^{\mathcal{P}_3})\mathbf{m} + \sigma_c^2\mathbf{w}_{k,u}^H\mathbf{w}_{k,u}} \geq \eta,\forall k,\forall u. \end{cases} \tag{41}$$

This subproblem is similar to the previous $\mathcal{P}_{2.1}$ and hence it can be also solved by Algorithm 1 with variables appropriately substituted. Notice that, based on the inequality (35), the objective value in (39) is always equal or great than the simplified problem (41) which guarantees the monotonic increasing of radar SINR in the MM iteration.

D. Subproblem 4: Update of Passive Beamformer

With $\mathbf{w}_{k,t}$, $\mathbf{w}_{k,u}$, $\mathbf{f}_k$, $\mathbf{M}$ fixed, the subproblem with respect to the phase-shift design is

$$\mathcal{P}_4\begin{cases} \underset{\boldsymbol{\phi},\boldsymbol{\varphi}}{\text{maximize}}\ \min_t \text{SINR}_{R_t} \\ \text{subject to}\quad |\boldsymbol{\phi}| = 1,\ |\boldsymbol{\varphi}| = 1,\ \boldsymbol{\phi} = \boldsymbol{\varphi} \\ \frac{\boldsymbol{\phi}^T\mathbf{\Sigma}_{k,u}^{\mathcal{P}_4}\boldsymbol{\phi}^* + 2\Re(\boldsymbol{\phi}^T\mathbf{d}_{k,u}^{\mathcal{P}_4}) + d_{k,u}^{\mathcal{P}_4}}{\boldsymbol{\phi}^T\widetilde{\mathbf{\Sigma}}_{k,u}^{\mathcal{P}_4}\boldsymbol{\phi}^* + 2\Re(\boldsymbol{\phi}^T\widetilde{\mathbf{d}}_{k,u}^{\mathcal{P}_4}) + \tilde{d}_{k,u}^{\mathcal{P}_4}} \geq \eta \quad \forall k \quad \forall u \end{cases} \tag{42}$$

where $\boldsymbol{\phi} = \mathbf{\Phi}^T\mathbf{1}_{N_R}$ denotes the phase-shift vector; $\boldsymbol{\varphi}$ denotes the auxiliary variable; $d_{k,u}^{\mathcal{P}_4}$, $\mathbf{d}_{k,u}^{\mathcal{P}_4}$, $\mathbf{\Sigma}_{k,u}^{\mathcal{P}_4}$, $\tilde{d}_{k,u}^{\mathcal{P}_4}$, $\widetilde{\mathbf{d}}_{k,u}^{\mathcal{P}_4}$, and $\widetilde{\mathbf{\Sigma}}_{k,u}^{\mathcal{P}_4}$ are defined as follows:

$$d_{k,u}^{\mathcal{P}_4} = \mathbf{w}_{k,u}^H\mathbf{H}_{C_u,k}^{\text{dir}}\mathbf{M}\mathbf{V}_k\mathbf{f}_k\mathbf{\Lambda}_u(\mathbf{w}_{k,u}^H\mathbf{H}_{C_u,k}^{\text{dir}}\mathbf{M}\mathbf{V}_k\mathbf{f}_k)^H \tag{43a}$$

$$\mathbf{d}_{k,u}^{\mathcal{P}_4} = \langle \mathbf{w}_{k,u}^H\mathbf{H}_{C_u,k}^{\text{RIS}}\rangle \mathbf{G}_k\mathbf{M}\mathbf{V}_k\mathbf{f}_k\mathbf{\Lambda}_u(\mathbf{w}_{k,u}^H\mathbf{H}_{C_u,k}^{\text{dir}}\mathbf{M}\mathbf{V}_k\mathbf{f}_k)^H \tag{43b}$$

$$\mathbf{\Sigma}_{k,u}^{\mathcal{P}_4} = \langle \mathbf{w}_{k,u}^H\mathbf{H}_{C_u,k}^{\text{RIS}}\rangle \mathbf{G}_k\mathbf{M}\mathbf{V}_k\mathbf{f}_k\mathbf{\Lambda}_u(\langle \mathbf{w}_{k,u}^H\mathbf{H}_{C_u,k}^{\text{RIS}}\rangle \mathbf{G}_k\mathbf{M}\mathbf{V}_k\mathbf{f}_k)^H \tag{43c}$$

$$\tilde{d}_{k,u}^{\mathcal{P}_4} = \mathbf{w}_{k,u}^H \mathbf{H}_{C_u,k}^{\text{dir}} \mathbf{M}\mathbf{V}_k \mathbf{f}_k \widetilde{\mathbf{\Lambda}}_u (\mathbf{w}_{k,u}^H \mathbf{H}_{C_u,k}^{\text{dir}} \mathbf{M}\mathbf{V}_k \mathbf{f}_k)^H \tag{43d}$$

$$\widetilde{\mathbf{d}}_{k,u}^{\mathcal{P}_4} = \langle \mathbf{w}_{k,u}^H \mathbf{H}_{C_u,k}^{\text{RIS}} \rangle \mathbf{G}_k \mathbf{M}\mathbf{V}_k \mathbf{f}_k \widetilde{\mathbf{\Lambda}}_u (\mathbf{w}_{k,u}^H \mathbf{H}_{C_u,k}^{\text{dir}} \mathbf{M}\mathbf{V}_k \mathbf{f}_k)^H \tag{43e}$$

$$\widetilde{\mathbf{\Sigma}}_{k,u}^{\mathcal{P}_4} = \langle \mathbf{w}_{k,u}^H \mathbf{H}_{C_u,k}^{\text{RIS}} \rangle \mathbf{G}_k \mathbf{M}\mathbf{V}_k \mathbf{f}_k \widetilde{\mathbf{\Lambda}}_u (\langle \mathbf{w}_{k,u}^H \mathbf{H}_{C_u,k}^{\text{RIS}} \rangle \mathbf{G}_k \mathbf{M}\mathbf{V}_k \mathbf{f}_k)^H. \tag{43f}$$

Accordingly, $\mathcal{P}_4$ is rewritten as

$$\mathcal{P}_{4.1} \begin{cases} \underset{\boldsymbol{\phi},\boldsymbol{\varphi}}{\text{maximize}} \ \min_t \frac{f_t(\boldsymbol{\phi},\boldsymbol{\varphi})}{g_t(\boldsymbol{\phi},\boldsymbol{\varphi})} \\ \text{subject to} \quad |\boldsymbol{\phi}| = 1, |\boldsymbol{\varphi}| = 1, \boldsymbol{\phi} - \boldsymbol{\varphi} = \mathbf{0} \\ \frac{\boldsymbol{\phi}^T \mathbf{\Sigma}_{k,u}^{\mathcal{P}_4} \boldsymbol{\phi}^* + 2\Re(\boldsymbol{\phi}^T \mathbf{d}_{k,u}^{\mathcal{P}_4}) + d_{k,u}^{\mathcal{P}_4}}{\boldsymbol{\phi}^T \widetilde{\mathbf{\Sigma}}_{k,u}^{\mathcal{P}_4} \boldsymbol{\phi}^* + 2\Re(\boldsymbol{\phi}^T \widetilde{\mathbf{d}}_{k,u}^{\mathcal{P}_4}) + \tilde{d}_{k,u}^{\mathcal{P}_4}} \geq \eta \quad \forall k \quad \forall u \end{cases} \tag{44}$$

where

$$\begin{aligned} f_t(\boldsymbol{\phi},\boldsymbol{\varphi}) &= \boldsymbol{\phi}^T \mathbf{\Sigma}_t^{\mathcal{P}_4}(\boldsymbol{\varphi}) \boldsymbol{\phi}^* + 2\Re(\boldsymbol{\phi}^T \mathbf{d}_t^{\mathcal{P}_4}(\boldsymbol{\varphi})) + d_t^{\mathcal{P}_4}(\boldsymbol{\varphi}) \\ &= \boldsymbol{\varphi}^T \mathbf{\Sigma}_t^{\mathcal{P}_4}(\boldsymbol{\phi}) \boldsymbol{\varphi}^* + 2\Re(\boldsymbol{\varphi}^T \mathbf{d}_t^{\mathcal{P}_4}(\boldsymbol{\phi})) + d_t^{\mathcal{P}_4}(\boldsymbol{\phi}) \end{aligned} \tag{45a}$$

$$\begin{aligned} g_t(\boldsymbol{\phi},\boldsymbol{\varphi}) &= \boldsymbol{\phi}^T \widetilde{\mathbf{\Sigma}}_t^{\mathcal{P}_4}(\boldsymbol{\varphi}) \boldsymbol{\phi}^* + 2\Re(\boldsymbol{\phi}^T \widetilde{\mathbf{d}}_t^{\mathcal{P}_4}(\boldsymbol{\varphi})) + \tilde{d}_t^{\mathcal{P}_4}(\boldsymbol{\varphi}) \\ &= \boldsymbol{\varphi}^T \widetilde{\mathbf{\Sigma}}_t^{\mathcal{P}_4}(\boldsymbol{\phi}) \boldsymbol{\varphi}^* + 2\Re(\boldsymbol{\varphi}^T \widetilde{\mathbf{d}}_t^{\mathcal{P}_4}(\boldsymbol{\phi})) + \tilde{d}_t^{\mathcal{P}_4}(\boldsymbol{\phi}) \end{aligned} \tag{45b}$$

and $\mathbf{\Sigma}_t^{\mathcal{P}_4}(\boldsymbol{\varphi})$, $\mathbf{d}_t^{\mathcal{P}_4}(\boldsymbol{\varphi})$, $d_t^{\mathcal{P}_4}(\boldsymbol{\varphi})$, $\mathbf{\Sigma}_t^{\mathcal{P}_4}(\boldsymbol{\phi})$, $\mathbf{d}_t^{\mathcal{P}_4}(\boldsymbol{\phi})$, and $d_t^{\mathcal{P}_4}(\boldsymbol{\phi})$ are defined as

where $\tilde{\boldsymbol{\varphi}} = \text{diag}(\boldsymbol{\varphi})$, and the variables related to (45b) can be similarly defined as (45a) and, hence, omit it herein.

Rewriting the problem $\mathcal{P}_{4.1}$ as

$$\mathcal{P}_{4.2} \begin{cases} \underset{\boldsymbol{\phi},\boldsymbol{\varphi}}{\text{maximize}} \ \min_t f_t(\boldsymbol{\phi},\boldsymbol{\varphi}) - \lambda_{\mathcal{P}_4} g_t(\boldsymbol{\phi},\boldsymbol{\varphi}) \\ \text{subject to} \quad |\boldsymbol{\phi}| = 1, |\boldsymbol{\varphi}| = 1, \boldsymbol{\phi} - \boldsymbol{\varphi} = \mathbf{0} \\ \frac{\boldsymbol{\phi}^T \mathbf{\Sigma}_{k,u}^{\mathcal{P}_4} \boldsymbol{\phi}^* + 2\Re(\boldsymbol{\phi}^T \mathbf{d}_{k,u}^{\mathcal{P}_4}) + d_{k,u}^{\mathcal{P}_4}}{\boldsymbol{\phi}^T \widetilde{\mathbf{\Sigma}}_{k,u}^{\mathcal{P}_4} \boldsymbol{\phi}^* + 2\Re(\boldsymbol{\phi}^T \widetilde{\mathbf{d}}_{k,u}^{\mathcal{P}_4}) + \tilde{d}_{k,u}^{\mathcal{P}_4}} \geq \eta \quad \forall k \quad \forall u \end{cases} \tag{46}$$

where $\lambda_{\mathcal{P}_4} = \min_t \frac{f_t(\boldsymbol{\phi},\boldsymbol{\varphi})}{g_t(\boldsymbol{\phi},\boldsymbol{\varphi})}$ denotes the Dinkelbach parameter. According to [68], we have the following inequality:

$$\boldsymbol{\phi}^H \mathbf{H} \boldsymbol{\phi} \leq 2\Re(\boldsymbol{\phi}^{(l)H} (\mathbf{H} - \zeta) \boldsymbol{\phi}) + 2\zeta N_R - \boldsymbol{\phi}^{(l)H} \mathbf{H} \boldsymbol{\phi}^{(l)} \tag{47}$$

where $|\boldsymbol{\phi}| = 1$, $\mathbf{H}$ is the PSD matrix $\zeta \geq \lambda_{\max}(\mathbf{H})$, $\boldsymbol{\phi}^{(l)}$ denotes the current point (at the lth iteration), and the equality holds if and only if $\boldsymbol{\phi} = \boldsymbol{\phi}^{(l)}$. Then, we can further rewrite and simplify $\mathcal{P}_{4.2}$ as [40]

$$\mathcal{P}_{4.3} \begin{cases} \underset{\boldsymbol{\phi},\boldsymbol{\varphi}}{\text{minimize}} \ \max_{\|\mathbf{z}\|_1=1} \sum_{t=1}^T z_t (\lambda_{\mathcal{P}_4} g_t(\boldsymbol{\phi},\boldsymbol{\varphi}) - \hat{f}_t(\boldsymbol{\phi},\boldsymbol{\varphi})) \\ \text{subject to } |\boldsymbol{\phi}| = 1, |\boldsymbol{\varphi}| = 1, \boldsymbol{\phi} - \boldsymbol{\varphi} = \mathbf{0} \\ 2\Re(\boldsymbol{\phi}^T \mathbf{p}_{k,u}^{\mathcal{P}_4}) \leq p_{k,u} \quad \forall k \quad \forall u \end{cases} \tag{48}$$

where $\mathbf{z} = [z_1, \ldots, z_T]^T \succeq \mathbf{0}$ denotes the weight vector for selecting the maximum objective function over different targets, $\hat{f}_t(\boldsymbol{\phi},\boldsymbol{\varphi})$ is the right-hand side of inequality (35), and thus, a lower bound function of $f_t(\boldsymbol{\phi},\boldsymbol{\varphi})$, $p_{k,u}$ and $\mathbf{p}_{k,u}$ are the reconstructed scalar and vector to linearize the SINR constraint

$$\mathbf{p}_{k,u} = 2\eta(\widetilde{\mathbf{\Sigma}}_{k,u}^{\mathcal{P}_4} - \zeta_{k,u}) \boldsymbol{\phi}_{l_4}^* + 2\eta \widetilde{\mathbf{d}}_{k,u}^{\mathcal{P}_4} - 2\mathbf{\Sigma}_{k,u}^{\mathcal{P}_4} \boldsymbol{\phi}_{l_4}^* - 2\mathbf{d}_{k,u}^{\mathcal{P}_4} \tag{49a}$$

$$p_{k,u} = \eta(\boldsymbol{\phi}_{l_4}^H (\widetilde{\mathbf{\Sigma}}_{k,u}^{\mathcal{P}_4})^T \boldsymbol{\phi}_{l_4} - 2\zeta_{k,u} N_R - \tilde{d}_{k,u}^{\mathcal{P}_4}) + d_{k,u}^{\mathcal{P}_4} - \text{const.} \tag{49b}$$

where the constant is $\boldsymbol{\phi}_{l_4}^H (\mathbf{\Sigma}_{k,u}^{\mathcal{P}_4})^T \boldsymbol{\phi}_{l_4}$. Then, the augmented Lagrangian function of (48) is

$$\begin{aligned} \mathcal{L}(\boldsymbol{\phi}, \boldsymbol{\psi}, \mathbf{u}, \mathbf{w}, \rho) = &\max_{\|\mathbf{z}\|_1=1} \sum_{t=1}^T z_t (\lambda_{\mathcal{P}_4} g_t(\boldsymbol{\phi},\boldsymbol{\varphi}) - \hat{f}_t(\boldsymbol{\phi},\boldsymbol{\varphi})) \\ &+ \frac{\rho}{2} \|\boldsymbol{\phi} - \boldsymbol{\psi} + \mathbf{u}\|_2^2 + \Re\{\mathbf{w}^T \mathbf{c}\} \end{aligned} \tag{50}$$

where ρ is the penalty parameter, $\mathbf{u}$ and $\mathbf{w}$ denote the auxiliary variables, and $\mathbf{c} = [c_1, \ldots, c_U]^T$, in which $c_u = 2\Re(\boldsymbol{\phi}^T \mathbf{p}_u^{\mathcal{P}_4}) - p_u$. Then, as the previous work problem [40], $\mathcal{P}_{4.3}$ is solved by the C-ADMM algorithm which is summarized in Algorithm 2. Noted that in each ADMM iteration, the nonconvex unit-sphere programming (51) and (52) can be directly solved by the RSD algorithm; see details in [39].

Algorithm 2: C-ADMM Algorithm to Solve $\mathcal{P}_{4.1}$.

Input: ϵ_2, $\mathbf{u}$, $\mathbf{w}$, and $\boldsymbol{\phi}^{(l)}$
Output: $\boldsymbol{\phi}^{(l+1)} = \boldsymbol{\phi}_{l_4}$.
1: Set $l_4 = 0$, $\boldsymbol{\psi}_0 = \boldsymbol{\phi}_0 = \boldsymbol{\phi}^{(l)}$;
2: **repeat**
3: Compute: $\lambda_{\mathcal{P}_4}^{(l_4)} = \min_t \frac{f_t(\boldsymbol{\phi},\boldsymbol{\varphi})}{g_t(\boldsymbol{\phi},\boldsymbol{\varphi})}$;
4: Update $\mathbf{z}$ by solving the problem (48), which is convex w.r.t. the variable $\mathbf{z}$;
5: Update $\boldsymbol{\phi}_{l_4}$ via solving

$$\underset{\boldsymbol{\phi}}{\text{minimize}} \ \mathcal{L}(\boldsymbol{\phi}, \boldsymbol{\psi}^{(l_4)}, \mathbf{u}, \mathbf{w}, \rho), \ \text{subject to } |\boldsymbol{\phi}| = 1. \tag{51}$$

6: Update $\boldsymbol{\psi}_{l_4}$ via solving

$$\underset{\boldsymbol{\psi}}{\text{minimize}} \ \mathcal{L}(\boldsymbol{\phi}^{(l_4+1)}, \boldsymbol{\psi}, \mathbf{u}, \mathbf{w}, \rho), \ \text{subject to } |\boldsymbol{\psi}| = 1. \tag{52}$$

7: Update the dual variable $\mathbf{u}$ and $\mathbf{w}$;
8: $l_4 \leftarrow l_4 + 1$;
9: **until** $\|\boldsymbol{\phi}_{l_4+1} - \boldsymbol{\phi}_{l_4}\|_2^2 \leq \epsilon_2$ or reach the maximum iteration;
11: **return** $\boldsymbol{\phi}_{l_4}$;

Based on the above, the proposed AM algorithm for the optimization problem (25) is summarized in Algorithm 3.

REMARK 3 The optimization framework is general and can handle different architectures by appropriate constraints on $\mathbf{M}$ and choice of $\mathbf{V}$. In particular, letting $N_{RF} = N_{\text{Tx}}$, and $\mathbf{M} = \mathbf{V} = \mathbf{I}_{N_{RF}}$, the problem reduces to classical digital beamforming-based DFRC. Further, letting $\mathbf{M} = \mathbf{I}$ and different choices of $\mathbf{V}$ leads to different hybrid analog–digital beamforming architectures, including partial and fully connected.

E. Computational Complexity

The overall computational burden of Algorithm 3 is linear with the number of outer iterations. Meanwhile, at each outer iteration, the closed-form solution of the radar filter $\mathbf{w}_{k,t}, t = 1, \ldots, T$ and receive combiner $\mathbf{w}_{k,u}$,

Algorithm 3: Alternating Maximization Algorithm to Solve (25).

Input: ϵ_3, $\mathbf{w}_t^{(l)}$, $\mathbf{w}_u^{(l)}$, $\mathbf{f}^{(l)}$, $\mathbf{M}^{(l)}$ and $\boldsymbol{\phi}^{(l)}$.

Output: $\mathbf{w}_t^\star = \mathbf{w}_t^{(l)}$, $\mathbf{w}_u^\star = \mathbf{w}_u^{(l)}$, $\mathbf{f}_k^\star = \mathbf{f}_k^{(l)}$, $\mathbf{M}^\star = \mathbf{M}^{(l)}$ and $\boldsymbol{\Phi}^\star = \boldsymbol{\Phi}^{(l)}$.

1: Set $l = 0$;
2: **repeat**
3: Update $\boldsymbol{\phi}^{(l)}$ via Algorithm 2 and reconstruct $\boldsymbol{\Phi}^{(l)}$;
4: Update $\mathbf{w}_t^{(l)}$ and $\mathbf{w}_u^{(l)}$ as (31a) and (31b), respectively;
5: Update $\mathbf{f}^{(l)}$ via Algorithm 1 and reconstruct $\mathbf{f}_k^{(l)}$;
6: Update $\mathbf{M}^{(l)}$ via Algorithm 1 by changing the input variables;
7: $l \leftarrow l + 1$;
8: **until** $(\min_t \mathrm{SINR}_{R_t}^{(l)} - \min_t \mathrm{SINR}_{R_t}^{(l-1)})^2 \le \epsilon_3$ or maximum iteration reached;
9: **return** $\mathbf{w}_t^{(l)}$, $\mathbf{w}_u^{(l)}$, $\mathbf{f}_k^{(l)}$, $\mathbf{M}^{(l)}$, and $\boldsymbol{\Phi}^{(l)}$;

$u = 1, \ldots, U$ is given by solving the GRQ problem with the complexity of the order of $\mathcal{O}(TN_{\mathrm{Rx}}^3 + UN_U^3)$. Then, for the update of the transmit beamforming matrix $\mathbf{f}_k$, $k = 1, \ldots, K$, the computational cost of Algorithm 1 is linear with the number of inner iterations l_2. At each inner iteration of the Dinkelbach-based method, the problem is solved by the CVX [69] with the complexity of $\mathcal{O}(K^3 N_{\mathrm{RF}}^3 U^3)$. Similarly, for the update of the holographic beamforming matrix $\mathbf{M}$, the complexity is $\mathcal{O}(N_{\mathrm{Tx}}^3)$. In order to update the phase-shift matrix $\boldsymbol{\Phi}$ in Algorithm 2, the C-ADMM and RSD algorithms are combined with the total complexity $\mathcal{O}(l_4(2l_3N_R^2 + N_R^2))$, where l_3 and l_4 denote the maximum iteration number of RSD and C-ADMM, respectively. Finally, the total complexity of the proposed algorithm is $\mathcal{O}(TN_B^2 + UN_U^2 + K^3N_{RF}^3U^3 + N_B^3 + l_4(2l_3N_R^2 + N_R^2))$ for each outer iteration.

IV. NUMERICAL EXPERIMENTS

A. Simulation Set Up

We validated our models and methods through extensive numerical experiments based on the parameter in Table I. Unless otherwise specified, in the simulations, RHS, RIS, and MU are equipped with the square UPA with $N_{\mathrm{Tx}} = 25$, $N_R = 64$, and $N_U = 16$ elements, respectively. Meanwhile, DFBS equips $N_{\mathrm{RF}} = 4$ feeds, which are connected with RHS. As shown in Fig. 3, we deploy a DFBS at the 3-D position $\mathbf{p}_B = [0\,\mathrm{m}, 0\,\mathrm{m}, 3\,\mathrm{m}]$ and an RIS at $\mathbf{p}_R = [5\,\mathrm{m}, 0\,\mathrm{m}, 5\,\mathrm{m}]$. Two targets are located at $\mathbf{p}_T(1) = [5\,\mathrm{m}, 0\,\mathrm{m}, 0\,\mathrm{m}]$, and $\mathbf{p}_T(2) = [7\,\mathrm{m}, 0\,\mathrm{m}, 4\,\mathrm{m}]$, three clutter discretes are at $\mathbf{p}_C(1) = [9\,\mathrm{m}, -3\,\mathrm{m}, 0\,\mathrm{m}]$, $\mathbf{p}_C(2) = [12\,\mathrm{m}, -3\,\mathrm{m}, 1\,\mathrm{m}]$, and $\mathbf{p}_C(3) = [15\,\mathrm{m}, -3\,\mathrm{m}, 1\,\mathrm{m}]$, respectively. Meanwhile, we consider three users ($U = 3$) located at $\mathbf{p}_U(1) = [3\,\mathrm{m}, 6\,\mathrm{m}, 0\,\mathrm{m}]$, $\mathbf{p}_U(2) = [6\,\mathrm{m}, 6\,\mathrm{m}, 0\,\mathrm{m}]$, and $\mathbf{p}_U(3) = [9\,\mathrm{m}, 6\,\mathrm{m}, 0\,\mathrm{m}]$, respectively.

We consider that the central frequency of the wideband DFRC $f_c = 10$ GHz and the subcarrier spacing of OFDM is set to $\triangle f = 20$ MHz [60]. In the existing and emerging communications standards (LTE, LTE/A, and 5G NR), a physical resource block comprising 12 subcarriers and a number of OFDM symbols forms the basis for resource allocation. Motivated by this, we consider the subcarrier number $K = 16$ in our study. The Rician factor for the both RHS-user link and RIS-user link are set as $\Upsilon_{C_u}^{\mathrm{dir}} = \Upsilon_{C_u}^{\mathrm{RIS}} = 10$. The interelement spacing for the RHS, RIS, and MU are set as $\lambda_c/4$, $\lambda_c/2$, and $\lambda_c/2$, respectively, alone with both x- and y-axis. Finally, we set the refractive index of the RHS as $\gamma = \sqrt{3}$; see [35].

As indicated earlier, the distance-dependent path loss model is considered, i.e., $g = \sqrt{K_0(\frac{r_0}{r})^\epsilon}$ for both radar and communications paths. The signal attenuation is set as $K_0 = -30$ dB at the reference distance $r_0 = 1$ m. The relative distance of the DFBS-tth target, RIS-tth target, DFBS-qth clutter, RIS-qth clutter, DFBS-uth user, RIS-uth user, and DFBS-RIS, are, respectively, given by

$$r_{Bt} = \|\mathbf{p}_B - \mathbf{p}_T(t)\|_2, \quad r_{Rt} = \|\mathbf{p}_R - \mathbf{p}_T(t)\|_2 \tag{53a}$$
$$r_{Bq} = \|\mathbf{p}_B - \mathbf{p}_C(q)\|_2, \quad r_{Rq} = \|\mathbf{p}_R - \mathbf{p}_C(q)\|_2 \tag{53b}$$
$$r_{Bu} = \|\mathbf{p}_B - \mathbf{p}_U(u)\|_2, \quad r_{Ru} = \|\mathbf{p}_R - \mathbf{p}_U(u)\|_2 \tag{53c}$$
$$r_{BR} = \|\mathbf{p}_B - \mathbf{p}_R\|_2, \quad \forall t \quad \forall q \text{ and } \forall u. \tag{53d}$$

The corresponding path loss exponents are given by $\epsilon_{\mathrm{BR,LoS}} = 2.8$, $\epsilon_{Bu,\mathrm{LoS}} = 3.2$, $\epsilon_{Bu,\mathrm{NLoS}} = 3.6$, $\epsilon_{Ru,\mathrm{LoS}} = 3.0$, $\epsilon_{Ru,\mathrm{NLoS}} = 3.6$, $\epsilon_{Bt} = 3.2$, $\epsilon_{Bq} = 3.2$, $\epsilon_{Rt} = 3.0$, and

TABLE I
Simulation Parameters Setting

Parameter	Symbol	Value
Central frequency	f_c	10 GHz
Subcarrier spacing	$\triangle f$	20 MHz
Transmit power at each subcarrier	$\mathcal{P}_k$	1∼9 dBW
No. of RHS elements	N_{Tx}	16∼100
No. of MIMO array elements	N_{Rx}	16
No. of RIS elements	N_R	4∼64
No. of User elements	N_u	16
No. of downlink UEs	U	2∼6
No. of clutter patches	Q	3
No. of subcarriers	K	8∼64
No. of feeds	N_{RF}	4
Rician factor of DFBS(Tx)-user link	$\Upsilon_{C_u}^{\mathrm{dir}}$	10
Rician factor of RIS-user link	$\Upsilon_{C_u}^{\mathrm{RIS}}$	10
Refractive index of RHS	γ	$\sqrt{3}$
Radar noise power	σ_r^2	-65 dBm
Communications noise power	σ_c^2	-65 dBm
Communications SINR threshold	η	0∼36 dB

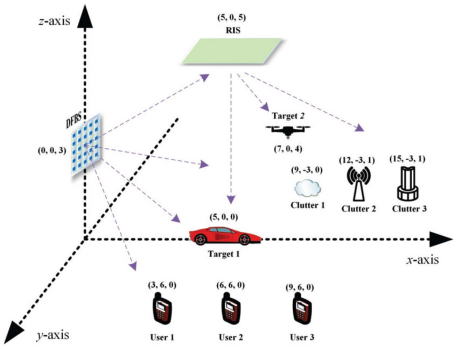

Fig. 3. Illustration of the simulation setup.

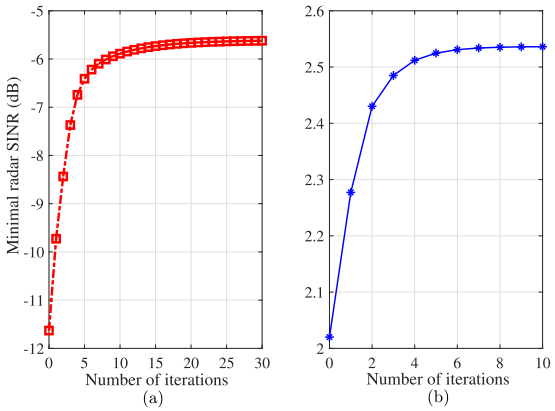

Fig. 4. Convergence performance of the inner iterations. (a) Minimum radar SINR versus the number of iterations for C-ADMM. (b) Minimum radar SINR versus the number of iterations for the Dinkelbach-based algorithm.

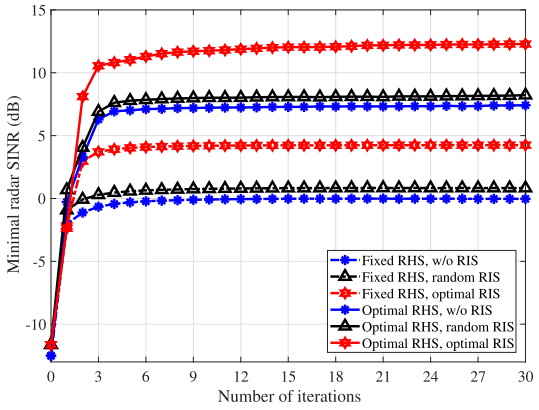

Fig. 5. Minimum radar SINR versus the number of outer iterations for AM.

$\epsilon_{Rq} = 3.0$. Based on the above, the fading component, i.e., channel gain for DFBS-target ($g_{Bt,k}$), RIS-target ($g_{Rt,k}$), DFBS-clutter ($g_{Bq,k}$), RIS-clutter ($g_{Rq,k}$), DFBS-user ($g_{Bu,k}$), RIS-user ($g_{Ru,k}$), and DFBS-RIS ($g_{BR,k}$) are obtained by appropriate substitution for ϵ and r into the expression (17) and (23). Without loss of the generality, the RCS of targets and clutters are set as $\alpha_t = 1$ and $\alpha_q = 1$, respectively. The transmit power at each subcarrier is set to $\mathcal{P}_k = 1$ dBw $\forall k$ and the noise variances are set to $\sigma_R^2 = -65$ dBm and $\sigma_C^2 = -65$ dBm for radar and communication, respectively. Meanwhile, the communication SINR threshold is set as $\eta = 12$ dB for all users and subcarriers. The termination threshold for the AM algorithm is set as $\epsilon_3 = 10^{-4}$. The initialization of $\mathbf{\Phi}^{(0)}$ is a randomly generated diagonal matrix, whose entries are assumed to be constant modulus with random phase shifts. The maximum iteration for Dinkelbach, C-ADMM, AM, and RSD are set as 10, 30, 30, and 100, respectively. We implement Algorithm 3 with 20 times random initialization and channel realizations due to the nonconvexity of problem (25) and then, for each figure, the achieved radar SINR is obtained by averaging those 20 independent experiments. All the simulations are performed on a standard PC [with Intel(R) Core(TM) i7-10610U CPU and 16.0 GB RAM].

B. Convergence of the Proposed Algorithm

First, we will evaluate the convergence performance of the inner iterations. Fig. 4(a) illustrates the convergence of the C-ADMM algorithm for solving the subproblem related to the RIS phase-shift design in the first AM iteration. It is seen that, as the iteration increases, the objective value of problem (25), i.e., minimum radar SINR, is monotonically improved and convergent within 30 iterations. Similarly, Fig. 4(b) expresses the convergence of the Dinkelbach-based method for tackling the subproblem of the digital beamformer design. It is observed that the Dinkelbach-based algorithm can be convergent within ten iterations.

Fig. 5 demonstrates the overall convergence of the proposed AM algorithm in different scenarios as follows.

TABLE II
Comparison of the running time for solving each subproblem in one iteration

Subproblem	Running time	Subproblem	Running time
$\mathcal{P}_1$	0.1170 s	$\mathcal{P}_3$	2.7500 s
$\mathcal{P}_2$	4.9460 s	$\mathcal{P}_4$	1.6620 s

1) *"Fixed RHS, w/o RIS"* involves optimal receive filter, digital beamforming, random RHS, and non-RIS, which are set as the *benchmark*.
2) *"Fixed RHS, Random RIS"* with optimal receive filter, digital beamforming, random RHS, and random RIS.
3) *"Fixed RHS, Optimal RIS"* comprises optimal receive filter, digital beamforming, random RHS, and optimal RIS.
4) *"Optimal RHS, w/o RIS"* involves optimal receive filter, digital beamforming, RHS, and non-RIS;
5) *"Optimal RHS, Random RIS"* with optimal receive filter, digital beamforming, RHS, and random RIS;
6). *"Optimal RHS, Optimal RIS"* comprises optimal receive filter, digital beamforming, RHS, and RIS.

Despite multiple linearization steps being implemented for both objective and constraint functions in the subproblems, the proposed AM algorithm is convergent in about 15 iterations. Meanwhile, the minimum radar SINR objective increases with the algorithm iteration since the objective value of the original problem is always greater than the linearized problem and the Dinkelbach method will converge to the optimal value for the linearized problem. The cases with the optimal RHS achieve the higher worst-case radar SINR compared with the random RHS. Meanwhile, with random phase shifts for RIS, the worst-case radar SINR is lower than that the optimal phase shifts but slightly higher than the non-RIS case. Meanwhile, the optimal phase shifts lead to at least 4- and 4.8-dB radar SINR gain for random RIS and non-RIS deployment, respectively.

To illustrate the efficiency of the algorithm, in Table II, the running time for solving each subproblem in the single

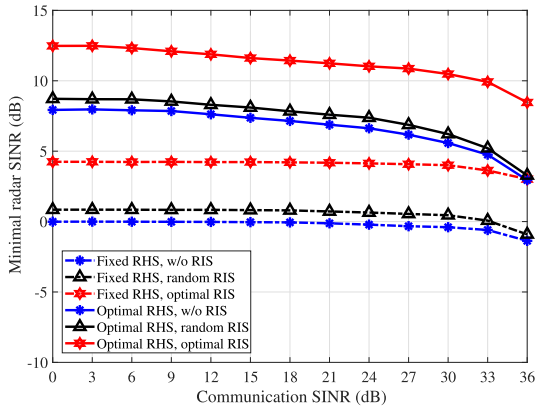

Fig. 6. Minimum Radar SINR versus communication SINR threshold.

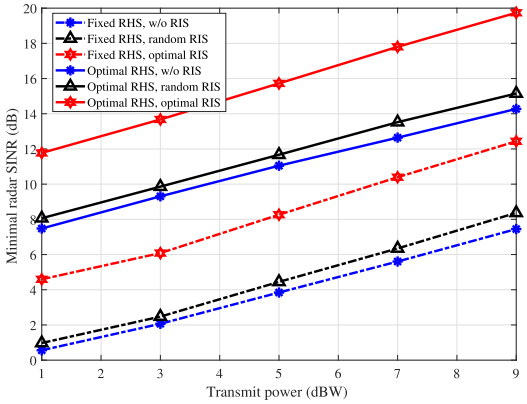

Fig. 7. Minimum Radar SINR versus the transmit power for each subcarrier.

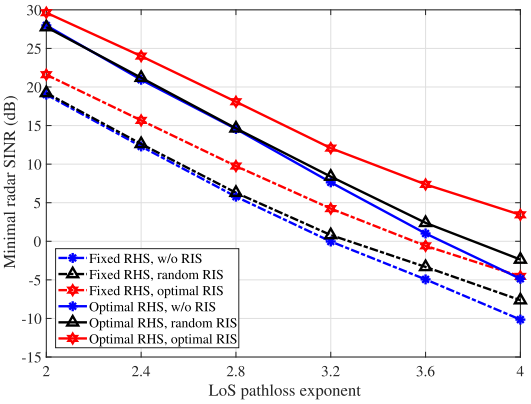

Fig. 8. Minimum Radar SINR versus radar direct LoS path loss.

iteration is presented. It is observed that most of the computational cost is on the subproblem of full-digital beamformer design $\mathcal{P}_2$. This is because the *frequency-dependent* digital beamformer should be properly designed for each subcarriers.

C. Performance Tradeoff between Communication and Radar

We illustrate the variation in the minimum achievable radar SINR with respect to different parameters to demonstrate the flexibility of our approach. In Fig. 6, the results of the minimum radar SINR versus the threshold of communication SINR η are illustrated. We vary the communications SINR threshold from 0 to 36 dB which covers the demands in most existing wireless applications. We observe that, in the DFRC system, the higher requirement on the communications SINR leads to the performance loss for minimum radar SINR. Hence, even with the assistance of RIS and RHS, the proposed holographic DFRC system still demonstrates a performance tradeoff between radar and communications, albeit, an enhanced one. Note that the threshold of communications SINR can be flexibly selected based on the requirement of the DFRC system, e.g., decoding performance or outage probability, and it can be also varied for different users and subcarriers.

D. Effect of Transmit Power

Fig. 7 shows the achievable minimal radar SINR versus the $\mathcal{P}_k$ for each subcarrier. Clearly, if we simultaneously optimize the receive filter, digital beamformer, holographic beamformer, and passive beamformer, the highest radar SINR is achieved compared with non-RIS, random RIS, and random RHS cases. Furthermore, for the RIS-assisted DFRC, the optimization of the holographic beamforming by RHS can provide around 3.7-dB SINR gain owing to its flexibility for controlling the radiation amplitude, and thus, the transmit beampattern. It is also observed that for all six cases (i.e., random RHS, optimized RHS, w/o RIS, random RIS, and optimized RIS), increasing of 1-dBW transmit power can bring around 2-dB radar SINR enhancement which indicates that, if we want to improve the radar SINR, one of the efficient ways is to increase the transmit power. Meanwhile, the proposed algorithm with both optimal RHS and RIS achieves the highest radar SINR which indicates the advantage of our proposed RIS-assisted holographic DFRC system.

E. Effect of Radar LoS Path Loss Exponent

Fig. 8 shows the achievable worst-case radar SINR versus radar LoS path loss exponent ϵ_{Bt} (i.e., direct path loss exponent between DFBS and target). The radar SINR is significantly reduced with the increase in the LoS path loss exponent. Further, in optimal RIS cases, optimizing RHS leads to around 7-dB radar SINR improvement which shows the importance of holographic beamformer design. Meanwhile, the proposed methods with optimal RIS and optimal RHS provide better radar SINR with the weak direct path, i.e., $\epsilon_{\text{dir}} \geq 3.6$. This demonstrates that RIS is more effective when a stable LoS path is missing.

F. Effect of Surface Element Number

Fig. 9(a), shows the achievable worst-case radar SINR versus RIS element number w.r.t x- (or y-) axis, N_x^R (or N_y^R). It is observed that random RIS cannot provide a stable performance enhancement compared with the optimal RIS, even with the larger element number. For example, when RIS element ranges from 4–9 total elements, random RIS does not offer any enhancement for both random RHS and optimal RHS. Different from that, the proposed method with the optimal RHS and RIS is able to enhance the system

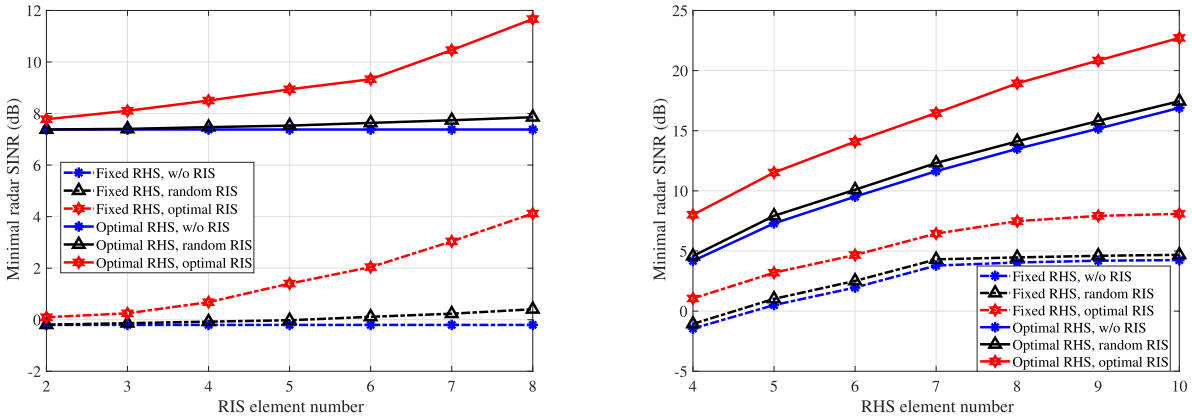

Fig. 9. Radar performance in terms of the element number of surfaces. (a) Minimum Radar SINR versus RIS element number. (b) Minimum Radar SINR versus RHS element number.

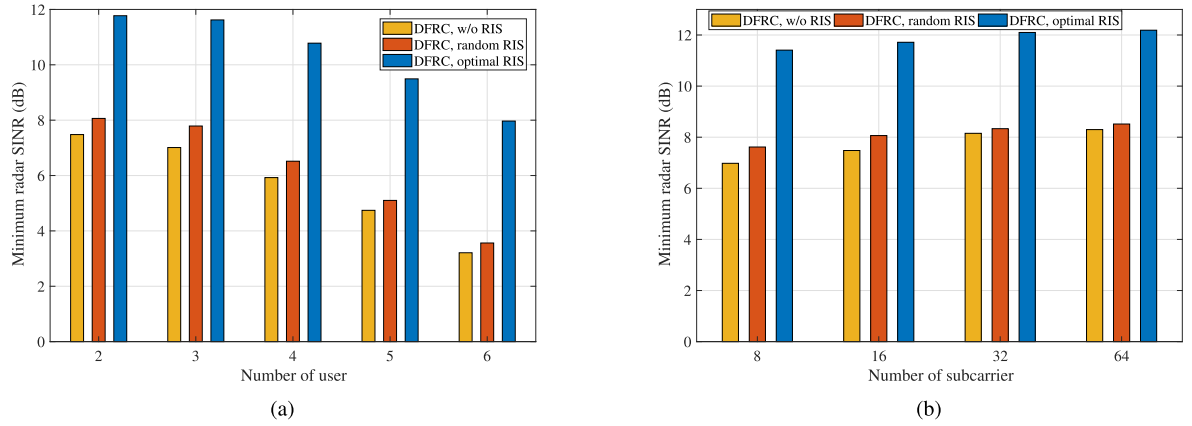

Fig. 10. Radar performance in terms of the number of users and subcarrier with optimal RHS. (a) Minimum Radar SINR versus user number. (b) Minimum Radar SINR versus subcarrier number.

continuously. Meanwhile, it is seen that each passive RIS element enhancement w.r.t x- (or y-) axis can offer around 0.4-dB SINR improvement under the optimal receive filter, digital beamforming, holographic beamforming, and passive beamforming, see *red curve*, when $N_x^R \leq 6$. And when $N_x^R > 6$, each passive RIS element can provide around 1-dB improvement. This kind of enhancement is crucial for holographic DFRC systems, especially in the dense environment, where the LoS components are weak. Fig. 9(b) shows the achievable worst-case radar SINR versus RHS element number w.r.t x- (or y-) axis, N_x^{Tx} (or N_y^{Tx}). With the increase in RHS elements, random RHS does not provide a stable radar SINR improvement, see the dot-dash curves. On the contrary, the case with optimal RHS and optimal RIS is able to enhance the system continuously which highlights the importance of the proposed joint design scheme for RIS-assisted holographic DFRC.

G. Effect of Number of Users and Subcarriers

Fig. 10(a) illustrates the achievable worst-case radar SINR w.r.t. the number of users. We observed again that the proposed method with the optimal RIS and RHS achieves the highest radar SINR compared with non-RIS, random-RIS, and random-RHS cases in terms of different user numbers. Meanwhile, the increase in communication users can also lead to the loss of radar SINR, and more communication users exacerbate this deterioration, e.g., $U = 6$. However, the proposed method with optimal RHS and RIS reaches the preferable radar SINR compared with the other counterparts.

Fig. 10(b) depicts the minimum radar SINR w.r.t the number of subcarriers. We observed that the increase of signal subcarrier and bandwidth can improve the radar performance. However, when the subcarrier number reaches a certain level, this improvement is negligible. This is because more communication SINR constraints should be satisfied simultaneously.

H. Radar Detection Performance

To further evaluate the receiver operating characteristic of radar, we calculate the radar detection probability as follows [55]:

$$P_d = \exp\left(\frac{\ln P_{\mathrm{fa}}}{1 + \mathrm{SINR}}\right) \tag{54}$$

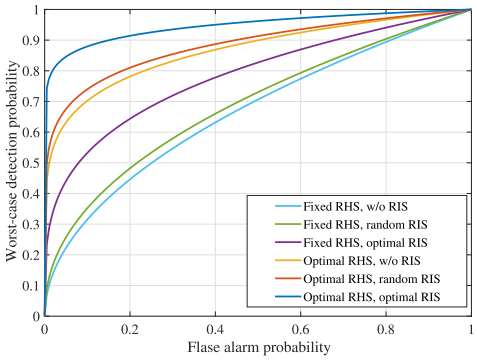

Fig. 11. Worst-case detection probability versus the false alarm probability.

where P_{fa} and P_d denote the false alarm and detection probability, respectively, and herein SINR denotes the minimum achieved SINR from the beamformer design. Fig. 11 depicts the achievable worst-case radar detection probability versus the false alarm probability. It is observed that with a certain false alarm probability, e.g., $P_{\text{fa}} = 0.1$, the proposed method with the optimal RHS and optimal RIS achieves the highest detection probability compared with the non-RIS, random RIS, and random RHS cases which highlights the superiority of our proposed RIS-aided holographic DFRC system.

V. CONCLUSION

In this article, we considered the joint deployment of the RHS and RIS to assist a wideband DFRC system with OFDM signaling. Our design of digital, holographic, and passive beamformers shows improvement in the performance of the DFRC system when compared with non-RIS and non-RHS systems. The key challenge to the design problem arises from the coupling of various parameters and nonconvexity. We showed that our AO approach facilitates not only decoupling but also a tractable design.

For highly dynamic wideband channels, machine learning methods may be employed to estimate the channel state [25]. This may also be incorporated with the RHS DFRC systems. A particularly complicated procedure in the RHS is the estimation of angle of arrivals because, unlike PAs whose feeds directly receive the signals, RHS feeds receive the signals after modulation by holographic patterns. This requires an additional maximum likelihood estimation step for AoA estimation.

Holographic DFRC is currently at an early stage of research. As a result, substantial challenges in prototyping, channel modeling, and optimized design remain. Graphene-based arrays and leaky-wave antennas are other alternatives for realizing these antenna structures [70]. Further, exploiting other non-OFDM multiple access technologies for signaling also offers a promising research avenue for holographic DFRC in the near future [35].

REFERENCES

[1] T. Wei, L. Wu, K. V. Mishra, and M. R. Bhavani Shankar, "RIS-aided wideband DFRC with reconfigurable holographic surface," in *Proc. IEEE Int. Conf. Acoust. Speech Signal Process.*, 2023, pp. 1–5.

[2] K. V. Mishra, A. M. Elbir, and A. I. Zaghloul, "Machine learning for metasurfaces design and their applications," in *Advances in Electromagnetics Empowered by Machine Learning*, (Electromagnetic Wave Theory and Applications) D. H. Werner and S. D. Campbell, Eds. Hoboken, NJ, USA: Wiley Press, 2022.

[3] Q. Wu and R. Zhang, "Towards smart and reconfigurable environment: Intelligent reflecting surface aided wireless network," *IEEE Commun. Mag.*, vol. 58, no. 1, pp. 106–112, Jan. 2020.

[4] J. A. Hodge, K. V. Mishra, and A. I. Zaghloul, "Intelligent time-varying metasurface transceiver for index modulation in 6G wireless networks," *IEEE Antennas Wireless Propag. Lett.*, vol. 19, no. 11, pp. 1891–1895, Nov. 2020.

[5] D. Sievenpiper, L. Zhang, R. F. Broas, N. G. Alexopolous, and E. Yablonovitch, "High-impedance electromagnetic surfaces with a forbidden frequency band," *IEEE Trans. Microw. Theory Techn.*, vol. 47, no. 11, pp. 2059–2074, Nov. 1999.

[6] H. Zhu, S. Cheung, K. L. Chung, and T. I. Yuk, "Linear-to-circular polarization conversion using metasurface," *IEEE Trans. Antennas Propag.*, vol. 61, no. 9, pp. 4615–4623, Sep. 2013.

[7] G. Minatti et al., "Modulated metasurface antennas for space: Synthesis analysis and realizations," *IEEE Trans. Antennas Propag.*, vol. 63, no. 4, pp. 1288–1300, Apr. 2015.

[8] K. V. Mishra, J. A. Hodge, and A. I. Zaghloul, "Reconfigurable metasurfaces for radar and communications systems," in *Proc. URSI Asia-Pacific Radio Sci. Conf.*, 2019, pp. 1–4.

[9] S. B. Glybovski, S. A. Tretyakov, P. A. Belov, Y. S. Kivshar, and C. R. Simovski, "Metasurfaces: From microwaves to visible," *Phys. Rep.*, vol. 634, pp. 1–72, 2016.

[10] Z. Esmaeilbeig, K. V. Mishra, and M. Soltanalian, "IRS-aided radar: Enhanced target parameter estimation via intelligent reflecting surfaces," in *Proc. IEEE Sensor Array Multichannel Signal Process. Workshop*, 2022, pp. 286–290.

[11] M. Di Renzo et al., "Smart radio environments empowered by reconfigurable intelligent surfaces: How it works, state of research, and the road ahead," *IEEE J. Sel. Areas Commun.*, vol. 38, no. 11, pp. 2450–2525, Nov. 2020.

[12] Q. Wu and R. Zhang, "Intelligent reflecting surface enhanced wireless network via joint active and passive beamforming," *IEEE Trans. Wireless Commun.*, vol. 18, no. 11, pp. 5394–5409, Nov. 2019.

[13] S. Buzzi, E. Grossi, M. Lops, and L. Venturino, "Foundations of MIMO radar detection aided by reconfigurable intelligent surfaces," *IEEE Trans. Signal Process.*, vol. 70, pp. 1749–1763, 2022.

[14] W. Tang et al., "Wireless communications with reconfigurable intelligent surface: Path loss modeling and experimental measurement," *IEEE Trans. Wireless Commun.*, vol. 20, no. 1, pp. 421–439, Jan. 2021.

[15] K. V. Mishra, A. Chattopadhyay, S. S. Acharjee, and A. P. Petropulu, "OptM3Sec: Optimizing multicast IRS-aided multiantenna DFRC secrecy channel with multiple eavesdroppers," in *Proc. IEEE Int. Conf. Acoust. Speech Signal Process.*, 2022, pp. 9037–9041.

[16] B. Watson and J. R. Guerci, *Non-Line-of-Sight Radar*. Norwood, MA, USA: Artech House, 2019.

[17] A. Aubry, A. De Maio, and M. Rosamilia, "Reconfigurable intelligent surfaces for N-LOS radar surveillance," *IEEE Trans. Veh. Technol.*, vol. 70, no. 10, pp. 10735–10749, Oct. 2021.

[18] H. Ur Rehman, F. Bellili, A. Mezghani, and E. Hossain, "Joint active and passive beamforming design for IRS-assisted multi-user MIMO systems: A VAMP-based approach," *IEEE Trans. Commun.*, vol. 69, no. 10, pp. 6734–6749, Oct. 2021.

[19] K. V. Mishra, M. B. Shankar, V. Koivunen, B. Ottersten, and S. A. Vorobyov, "Toward millimeter-wave joint radar communications: A signal processing perspective," *IEEE Signal Process. Mag.*, vol. 36, no. 5, pp. 100–114, Sep. 2019.

[20] A. M. Elbir, K. V. Mishra, M. R. B. Shankar, and S. Chatzinotas, "The rise of intelligent reflecting surfaces in integrated sensing and communications paradigms," *IEEE Netw.*, to be published, doi: 10.1109/MNET.128.2200446.

[21] T. Wei, L. Wu, K. V. Mishra, and M. R. B. Shankar, "Multi-IRS-aided Doppler-tolerant wideband DFRC system," *IEEE Trans. Commun.*, vol. 71, no. 11, pp. 6561–6577, Nov. 2023.
[22] Z.-M. Jiang et al., "Intelligent reflecting surface aided dual-function radar and communication system," *IEEE Syst. J.*, vol. 16, no. 1, pp. 475–486, Mar. 2022.
[23] X. Wang, Z. Fei, J. Huang, and H. Yu, "Joint waveform and discrete phase shift design for RIS-assisted integrated sensing and communication system under cramér-Rao bound constraint," *IEEE Trans. Veh. Technol.*, vol. 71, no. 1, pp. 1004–1009, Jan. 2022.
[24] T. Wei, L. Wu, K. V. Mishra, and S. M. R. Bhavani, "Simultaneous active-passive beamformer design in IRS-enabled multi-carrier DFRC system," in *Proc. Eur. Signal Process. Conf.*, 2022, pp. 1007–1011.
[25] A. M. Elbir, K. V. Mishra, and S. Chatzinotas, "Terahertz-band joint ultra-massive MIMO radar-communications: Model-based and model-free hybrid beamforming," *IEEE J. Special Topics Signal Process.*, vol. 15, no. 6, pp. 1468–1483, Nov. 2021.
[26] R.-B. R. Hwang, "Binary meta-hologram for a reconfigurable holographic metamaterial antenna," *Sci. Rep.*, vol. 10, no. 1, 2020, Art. no. 8586.
[27] R. Deng et al., "Reconfigurable holographic surfaces for future wireless communications," *IEEE Wireless Commun.*, vol. 28, no. 6, pp. 126–131, Dec. 2021.
[28] R. Deng, B. Di, H. Zhang, Y. Tan, and L. Song, "Reconfigurable holographic surface-enabled multi-user wireless communications: Amplitude-controlled holographic beamforming," *IEEE Trans. Wireless Commun.*, vol. 21, no. 8, pp. 6003–6017, Aug. 2022.
[29] F. Gholam, J. Via, and I. Santamaria, "Beamforming design for simplified analog antenna combining architectures," *IEEE Trans. Veh. Technol.*, vol. 60, no. 5, pp. 2373–2378, Jun. 2011.
[30] M. C. Johnson, S. L. Brunton, N. B. Kundtz, and J. N. Kutz, "Sidelobe canceling for reconfigurable holographic metamaterial antenna," *IEEE Trans. Antennas Propag.*, vol. 63, no. 4, pp. 1881–1886, Apr. 2015.
[31] T. Sleasman et al., "Waveguide-fed tunable metamaterial element for dynamic apertures," *IEEE Antennas Wireless Propag. Lett.*, vol. 15, pp. 606–609, 2016.
[32] X. Zhang, H. Zhang, H. Zhang, and B. Di, "Holographic radar: Target detection enabled by reconfigurable holographic surfaces," *IEEE Commun. Lett.*, vol. 27, no. 1, pp. 332–336, Jan. 2023.
[33] B. Di, "Reconfigurable holographic metasurface aided wideband OFDM communications against beam squint," *IEEE Trans. Veh. Technol.*, vol. 70, no. 5, pp. 5099–5103, May 2021.
[34] S. Zeng, H. Zhang, B. Di, H. Qin, X. Su, and L. Song, "Reconfigurable refractive surfaces: An energy-efficient way to holographic MIMO," *IEEE Commun. Lett.*, vol. 26, no. 10, pp. 2490–2494, Oct. 2022.
[35] H. Zhang et al., "Holographic integrated sensing and communication," *IEEE J. Sel. Areas Commun.*, vol. 40, no. 7, pp. 2114–2130, Jul. 2022.
[36] D. Dardari and N. Decarli, "Holographic communication using intelligent surfaces," *IEEE Commun. Mag.*, vol. 59, no. 6, pp. 35–41, Jun. 2021.
[37] Z. Wan, Z. Gao, F. Gao, M. D. Renzo, and M.-S. Alouini, "Terahertz massive MIMO with holographic reconfigurable intelligent surfaces," *IEEE Trans. Commun.*, vol. 69, no. 7, pp. 4732–4750, Jul. 2021.
[38] H. Li, W. Cai, Y. Liu, M. Li, Q. Liu, and Q. Wu, "Intelligent reflecting surface enhanced wideband MIMO-OFDM communications: From practical model to reflection optimization," *IEEE Trans. Commun.*, vol. 69, no. 7, pp. 4807–4820, Jul. 2021.
[39] K. Alhujaili, V. Monga, and M. Rangaswamy, "Transmit MIMO radar beampattern design via optimization on the complex circle manifold," *IEEE Trans. Signal Process.*, vol. 67, no. 13, pp. 3561–3575, Jul. 2019.
[40] J. Yang, G. Cui, X. Yu, and L. Kong, "Dual-use signal design for radar and communication via ambiguity function sidelobe control," *IEEE Trans. Veh. Technol.*, vol. 69, no. 9, pp. 9781–9794, Sep. 2020.
[41] S. E. Nai, W. Ser, Z. L. Yu, and H. Chen, "Beampattern synthesis for linear and planar arrays with antenna selection by convex optimization," *IEEE Trans. Antennas Propag.*, vol. 58, no. 12, pp. 3923–3930, Dec. 2010.
[42] R. Deng, B. Di, H. Zhang, and L. Song, "HDMA: Holographic-pattern division multiple access," *IEEE J. Sel. Areas Commun.*, vol. 40, no. 4, pp. 1317–1332, Apr. 2022.
[43] M. Wang, F. Gao, S. Jin, and H. Lin, "An overview of enhanced massive MIMO with array signal processing techniques," *IEEE J. Sel. Topics Signal Process.*, vol. 13, no. 5, pp. 886–901, Sep. 2019.
[44] J. Hu, Z. Chen, and J. Luo, "Multi-band reconfigurable holographic surface based ISAC systems: Design and optimization," in *Proc. IEEE Int. Conf. Commun.*, 2023, pp. 2927–2932, doi: 10.1109/ICC45041.2023.10279416.
[45] P. Wang, J. Fang, X. Yuan, Z. Chen, and H. Li, "Intelligent reflecting surface-assisted millimeter wave communications: Joint active and passive precoding design," *IEEE Trans. Veh. Technol.*, vol. 69, no. 12, pp. 14960–14973, Dec. 2020.
[46] B. Di, H. Zhang, L. Song, Y. Li, Z. Han, and H. V. Poor, "Hybrid beamforming for reconfigurable intelligent surface based multi-user communications: Achievable rates with limited discrete phase shifts," *IEEE J. Sel. Areas Commun.*, vol. 38, no. 8, pp. 1809–1822, Aug. 2020.
[47] M. Ding, P. Wang, D. López-Pérez, G. Mao, and Z. Lin, "Performance impact of LoS and NLoS transmissions in dense cellular networks," *IEEE Trans. Wireless Commun.*, vol. 15, no. 3, pp. 2365–2380, Mar. 2016.
[48] Z. Gao, C. Hu, L. Dai, and Z. Wang, "Channel estimation for millimeter-wave massive MIMO with hybrid precoding over frequency-selective fading channels," *IEEE Commun. Lett.*, vol. 20, no. 6, pp. 1259–1262, Jun. 2016.
[49] E. Vlachos, G. C. Alexandropoulos, and J. Thompson, "Wideband MIMO channel estimation for hybrid beamforming millimeter wave systems via random spatial sampling," *IEEE J. Sel. Topics Signal Process.*, vol. 13, no. 5, pp. 1136–1150, Sep. 2019.
[50] E. Shtaiwi, H. Zhang, S. Vishwanath, M. Youssef, A. Abdelhadi, and Z. Han, "Channel estimation approach for RIS assisted MIMO systems," *IEEE Trans. Cogn. Commun. Netw.*, vol. 7, no. 2, pp. 452–465, Jun. 2021.
[51] Y. Yang, B. Zheng, S. Zhang, and R. Zhang, "Intelligent reflecting surface meets OFDM: Protocol design and rate maximization," *IEEE Trans. Commun.*, vol. 68, no. 7, pp. 4522–4535, Jul. 2020.
[52] Z. Zhang and L. Dai, "A joint precoding framework for wideband reconfigurable intelligent surface-aided cell-free network," *IEEE Trans. Signal Process.*, vol. 69, pp. 4085–4101, 2021.
[53] S. Zhang and R. Zhang, "Capacity characterization for intelligent reflecting surface aided MIMO communication," *IEEE J. Sel. Areas Commun.*, vol. 38, no. 8, pp. 1823–1838, Aug. 2020.
[54] L. Wu et al., "A wideband amplifying reconfigurable intelligent surface," *IEEE Trans. Antennas Propag.*, vol. 70, no. 11, pp. 10623–10631, Nov. 2022.
[55] A. De Maio, S. De Nicola, Y. Huang, S. Zhang, and A. Farina, "Code design to optimize radar detection performance under accuracy and similarity constraints," *IEEE Trans. Signal Process.*, vol. 56, no. 11, pp. 5618–5629, Nov. 2008.
[56] L. Wu, P. Babu, and D. P. Palomar, "Transmit waveform/receive filter design for MIMO radar with multiple waveform constraints," *IEEE Trans. Signal Process.*, vol. 66, no. 6, pp. 1526–1540, Mar. 2018.
[57] Z. Cheng, B. Liao, Z. He, Y. Li, and J. Li, "Spectrally compatible waveform design for MIMO radar in the presence of multiple targets," *IEEE Trans. Signal Process.*, vol. 66, no. 13, pp. 3543–3555, Jul. 2018.
[58] Z. Cheng, Z. He, and B. Liao, "Hybrid beamforming for multi-carrier dual-function radar-communication system," *IEEE Trans. Cogn. Commun. Netw.*, vol. 7, no. 3, pp. 1002–1015, Sep. 2021.
[59] X. Liu, T. Huang, N. Shlezinger, Y. Liu, J. Zhou, and Y. C. Eldar, "Joint transmit beamforming for multiuser MIMO communications and MIMO radar," *IEEE Trans. Signal Process.*, vol. 68, pp. 3929–3944, 2020.

[60] Z. Cheng, Z. He, and B. Liao, "Hybrid beamforming design for OFDM dual-function radar-communication system," *IEEE J. Sel. Topics Signal Process.*, vol. 15, no. 6, pp. 1455–1467, Nov. 2021.
[61] X. Song, D. Zhao, H. Hua, T. X. Han, X. Yang, and J. Xu, "Joint transmit and reflective beamforming for IRS-assisted integrated sensing and communication," in *Proc. IEEE Wireless Commun. Netw. Conf.*, 2022, pp. 189–194.
[62] R. Liu, M. Li, Y. Liu, Q. Wu, and Q. Liu, "Joint transmit waveform and passive beamforming design for RIS-aided DFRC systems," *IEEE J. Sel. Topics Signal Process.*, vol. 16, no. 5, pp. 995–1010, Aug. 2022.
[63] M. Hua, Q. Wu, C. He, S. Ma, and W. Chen, "Joint active and passive beamforming design for IRS-aided radar-communication," *IEEE Trans. Wireless Commun.*, vol. 22, no. 4, pp. 2278–2294, Apr. 2023.
[64] S. Yu, L.-C. Tranchevent, B. De Moor, and Y. Moreau, *Rayleigh Quotient-Type Problems in Machine Learning*. Berlin, Germany: Springer, 2011, pp. 27–37.
[65] K. Shen, W. Yu, L. Zhao, and D. P. Palomar, "Optimization of MIMO device-to-device networks via matrix fractional programming: A minorization–maximization approach," *IEEE/ACM Trans. Netw.*, vol. 27, no. 5, pp. 2164–2177, Oct. 2019.
[66] T. Wei, L. Wu, and M. R. B. Shankar, "Joint waveform and precoding design for coexistence of MIMO radar and MU-MISO communication," *IET Signal Process.*, vol. 16, no. 7, pp. 788–799, 2022.
[67] A. Aubry, A. De Maio, and M. M. Naghsh, "Optimizing radar waveform and Doppler filter bank via generalized fractional programming," *IEEE J. Sel. Topics Signal Process.*, vol. 9, no. 8, pp. 1387–1399, Dec. 2015.
[68] J. Song, P. Babu, and D. P. Palomar, "Optimization methods for designing sequences with low autocorrelation sidelobes," *IEEE Trans. Signal Process.*, vol. 63, no. 15, pp. 3998–4009, Aug. 2015.
[69] M. Grant, S. Boyd, and Y. Ye, "CVX: MATLAB software for disciplined convex programming," Stanford Univ., Stanford, CA, USA, Tech. Rep., 2009.
[70] A. M. Elbir, K. V. Mishra, S. Chatzinotas, and M. Bennis, "Terahertz-band integrated sensing and communications: Challenges and opportunities," 2022, *arXiv:2208.01235*.

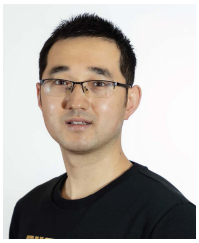

Tong Wei (Graduate Student Member, IEEE) received the B.E. degree in electronic science and technology from Hainan University, Hainan, China, and M.Sc. degree in electronic and communication engineering from Shenzhen University, Shenzhen, China, in 2017 and 2020, respectively. He is currently working toward the Ph.D. degree with the Interdisciplinary Centre for Security, Reliability and Trust (SnT), University of Luxembourg, Luxembourg City, Luxembourg.

His research interests include array signal processing, detection, and estimation theory, optimization with applications to wideband waveform design, integrated sensing and communication, and reconfigurable intelligent and holographic surfaces.

Linlong Wu (Senior Member, IEEE) received the B.E. degree in electronic information from Xian Jiaotong University, Xi'an, China, in 2014, and the Ph.D. degree in electronic and computer engineering from the Hong Kong University of Science and Technology, Hong Kong, in 2018.

He was with the wireless network group of Alibaba Cloud, Hangzhou, China, from 2018 to 2020, as a Research Engineer working on designing and building commercial RFID-based localization systems. Since 2020, he has been with the Interdisciplinary Centre for Security, Reliability and Trust, University of Luxembourg, Luxembourg City, Luxembourg, where he is currently a Research Scientist with the Signal Processing Applications in Radar and Communications group. His research interests are signal processing, optimization and machine learning with applications in waveform design, integrated sensing and communication and IoT networks.

Kumar Vijay Mishra (Senior Member, IEEE) received the B.Tech. degree summa cum laude (gold medal, honors) in electronics and communication engineering from the National Institute of Technology, Hamirpur, Himachal Pradesh, India in 2003, the M.S. degree in electrical engineering from Colorado State University, Fort Collins, CO, USA, in 2012, while working on NASAs Global Precipitation Mission Ground Validation (GPM-GV) weather radars, and the M.S. degree in mathematics and the Ph.D. degree in electrical engineering from the University of Iowa, Iowa City, IA, USA, in 2015.

He is currently the Senior Fellow with the United States Army Research Laboratory, Adelphi, MD, USA. He has coedited three upcoming books on radar: *Signal Processing for Joint Radar-Communications* (Wiley-IEEE Press), *Next-Generation Cognitive Radar Systems* (IET Press), and *Advances in Weather Radar* Volumes 1, 2 and 3 (IET Press), as the lead/corresponding co-editor. His research interests include radar systems, signal processing, remote sensing, and electromagnetics.

Dr. Mishra was the recipient of U. S. National Academies Harry Diamond Distinguished Fellowship from 2018 to 2021, Royal Meteorological Society Quarterly Journal Editors Prize in 2017, Viterbi Postdoctoral Fellowship in 2015 and 2016, Lady Davis Postdoctoral Fellowship in 2017, and DRDO LRDE Scientist of the Year Award in 2006. He has been the Vice-Chair of the newly constituted IEEE Synthetic Aperture Standards Committee of the IEEE Signal Processing Society, since 2021. Since 2020, he has been Associate Editor for IEEE TRANSACTIONS ON AEROSPACE AND ELECTRONIC SYSTEMS. He was the Vice Chair, from 2021 to 2023, and the Chair-designate, from 2023 to 2026, of International Union of Radio Science Commission C.

Bhavani Shankar M. R. (Senior Member, IEEE) received the masters and Ph.D. degrees in electrical communication engineering from the Indian Institute of Science, Bangalore, Karnataka, India, in 2000 and 2007 respectively.

He worked on Audio Coding algorithms as a Design Engineer with Sasken Communications, Bangalore, Karnataka, India, from 2000 to 2001. He was a Visiting Student with the Communication Theory Group, ETH Zurich, Zurich, Switzerland, headed by Prof. Helmut Bolcskei, during 2004. He was with Beceem Communications, Bangalore, Karnataka, India, from 2006 to 2007, as a Staff Design Engineer working on physical Layer algorithms for WiMAX compliant chipsets. He was a Post Doc with the ACCESS Linnaeus Centre, Signal Processing Lab, Royal Institute of Technology, Sweden, from 2007 to 2009. In 2009, he joined the Interdisciplinary Centre for Security, Reliability and Trust, University in Luxembourg, Luxembourg City, Luxembourg, as a Research Associate and is currently an Assistant Professor leading the Signal Processing Applications in Radar and Communications group. His research interests include design and optimization of MIMO communication systems, automotive radar and array processing, polynomial signal processing, satellite communication systems, resource allocation, game theory, and fast algorithms for structured matrices.

Dr. Shankar was the co-recipient of the 2014 Distinguished Contributions to Satellite Communications Award, from the Satellite and Space Communications Technical Committee of the IEEE Communications Society. He currently serves as handling Editor for *Elsevier Signal Processing*, and is on the Executive Committee of the IEEE Benelux joint chapter on communications and vehicular technology.